In-situ metrology for electrohydrodynamic inkjet printing towards micro/nano scale hybrid manufacturing

by

Benjamin Thomas Lies

A thesis submitted to the graduate faculty

in partial fulfillment of the requirements for the degree of

MASTER OF SCIENCE

Major: Industrial Engineering

Program of Study Committee:
Hantang Qin, Major Professor
Beiwen Li
Matthew Frank

The student author, whose presentation of the scholarship herein was approved by the program of study committee, is solely responsible for the content of this thesis. The Graduate College will ensure this thesis is globally accessible and will not permit alterations after a degree is conferred.

Iowa State University

Ames, Iowa

2019

TABLE OF CONTENTS

Page

LIST OF FIGURES

Page

Chapter 1

Chapter 2

Chapter 3

Chapter 4

Chapter 5

LIST OF TABLES

Page

Chapter 2

Chapter 4

ACKNOWLEDGMENTS

I would like to thank my major professor, Dr. Hantang Qin, and my committee members, Drs. Beiwen Li and Matt Frank, for their guidance and support throughout the course of this research. In addition, I would also like to thank my colleagues Sandeep Ravi-Kumar and Xiao Zhang for their assistance and patience during the writing process. I would like to thank the department faculty and staff for making my time at Iowa State University a wonderful experience.

ABSTRACT

This thesis lays the groundwork for a hybrid manufacturing system, combining laser ablation and electrohydrodynamic inkjet (e-jet) printing. A thorough review of laser ablation of polymers is provided. Trends and issues that arise during the process are noted and information essential to the choice of laser and polymer material is provided. In addition, methods were proposed for the in-process measurement of the E-jet printing system. The first method utilized machine vision and image processing to measure micro filament sizes. These filaments could be measured in real time and later converted into a 3D reconstruction. The second measures the resulted pattern prior to removal from the printing platform. Both of these processed allow for in-process measurements to be conducted which can be used for correction or characterization of the E-jet printing process. Currently, there are no such automated processes. Lastly, the use of a simple scalar diffraction setup to measure particle droplets was investigated. The issues which occurred during this investigation are discussed.

CHAPTER 1. GENERAL INTRODUCTION

Manufacturing is typically divided into three categories: additive manufacturing, subtractive manufacturing, and formative manufacturing. Additive manufacturing is a process which adds new material, typically in a layer by layer process, in order to create a part. Subtractive manufacturing is the process of material removal in order to create a new part. Lastly, formative manufacturing is the manipulation of a material to form a new part. Any combination of these three manufacturing processes is known as hybrid manufacturing. This work focuses on the use of light in hybrid manufacturing, specifically Electrohydrodynamic inkjet printing (additive) and laser ablation (subtractive).

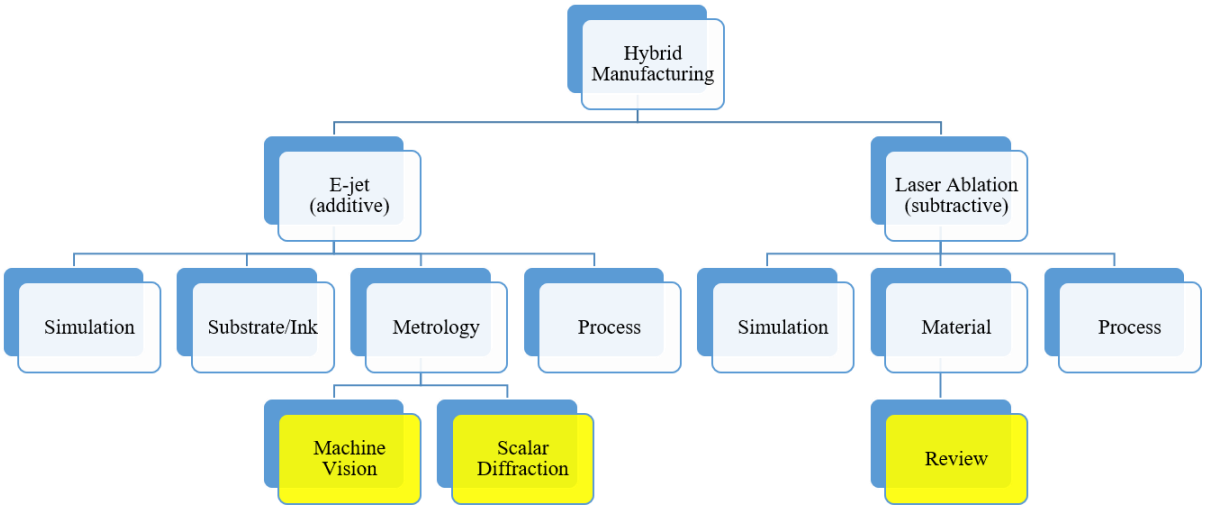

Figure 1: Hybrid manufacturing areas of interest. The highlighted sections were addressed in this work.

Electrohydrodynamic inkjet printing (e-jet printing) is a micro scale additive manufacturing method. E-jet printing was introduced after thermal and piezoelectric inkjet printing. Thermal inkjet printing utilizes a heating element which superheats an ink. This superheated ink then expands and forms a bubble which pushes ink out of a nozzle.

Piezoelectric inkjet printing utilizes a piezoelectric material which undergoes a change in shape when a charge is applied to it. This material expands and contracts with the charge, pushing ink out of the nozzle. E-jet printing utilizes a large electric potential between the nozzle and the substrate. This force draws the ink out in the formation of a Taylor cone. All of these inkjet printing methods have the advantages of high customization, flexible sample design and controllability however e-jet printing is the newest method and has the capability to produce the smallest feature size of the three methods. In addition to the smallest feature size, it has the capability to print metallic inks and polymers.

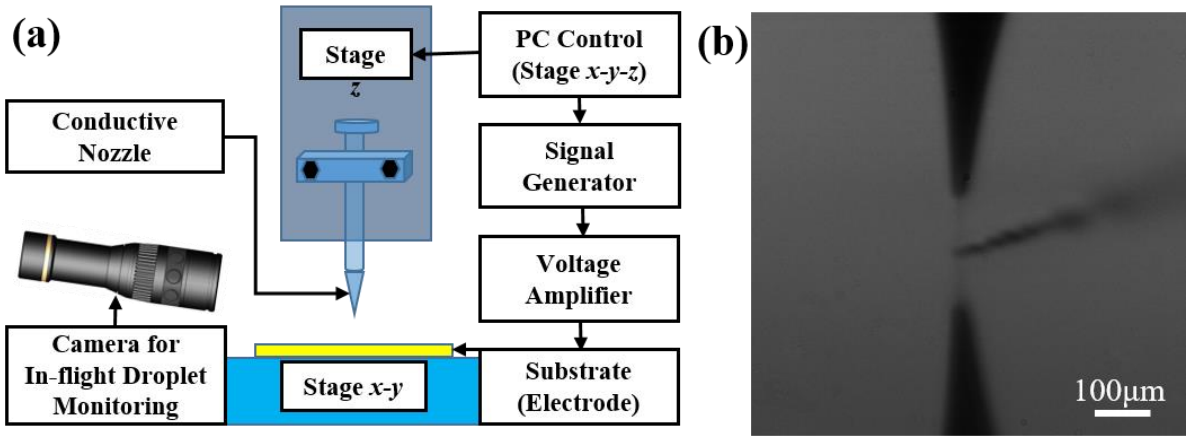

Figure 2: (a) The system setup for E-jet printing. (b) Taylor cone.

An example of an e-jet printing system is shown in Figure 2a. The x-y stage is a nanopositioning stage which ensures a very high degree of accuracy with regard to the placement of the material. The nozzle typically ranges from 10μm to 70μm. At such a small scale, the surface tension of the ink in the nozzle is very large, which requires a large force to overcome. A typical electric potential is between 200 volts and 2000 volts. This high voltage is the driving force for material expulsion through the nozzle. This potential difference is produced using a combination of a signal generator and a voltage amplifier. The resulting potential difference can vary from a DC voltage to a customized signal the operator designed.

Typically the voltage is either DC or an AC step function. The ink is drawn out from the nozzle where it takes the shape of a Taylor cone which can be viewed in Figure 2b. A Taylor cone has three distinct components, the cone, the jet, and the plume. The cone is the cone-shaped accumulation of material at the end of the nozzle. The jet is the filament shaped material emitted from the cone. The plume is the result of a jet breaking up into individual particles.

E-jet printing has several areas of ongoing research including simulation, substrate/ink studies, process control, and metrology. The studies regarding simulation focus on accurate prediction of a printed pattern given a set of process parameters. It leads into the study of process parameters where each variable in the process is measured, and the influence is characterized. These process parameters are amplitude/V_a, frequency/f, and waveform/V_w of applied voltage; viscosity/η, temperature/T, surface tension/σ of the ink; pressure/p, permittivity/ε of the space; standoff height/h, outside diameter/D_0, inside diameter/d_0, length/l, shape/S of the nozzle; and feedrate of printing/v. Two of those process parameters are the substrates and inks used, both of which are areas of study as well. Various substrates are being tested for their potential use in flexible electronics along with new ink compositions which can be used to print flexible circuitry. The last area of focus is the metrology of the process and resulting patterns. All of these areas of study are intertwined and are dependent on each other.

The focus of this work is on the exploration of the use of in-process metrology during the e-jet printing process. This means that the systems used to measure the process or resulting pattern should be able to do so while the printing process is taking place and without removal of the sample. The e-jet printing process has several features which may be

measured. From the Taylor cone, the jet and the plume may contain valuable information concerning the pattern printed. In addition to the Taylor cone, measuring the actual resulting pattern without removal from the printing stage is of great significance.

In this work, machine vision was used to measure the jetting section of the Taylor cone. This method was chosen as it is non-contact, relatively cheap, and can be used in the process. When the distance between the nozzle and substrate is small enough, the plume formation can be avoided altogether. The jetted material can then be used to characterize the size of the printed pattern. The second chapter of this work focuses on the characterization of the jet, mainly the size and volume of material. The image processing techniques used in this characterization are explained and the challenges encountered are discussed.

When the standoff distance is higher, the plume is formed and consist of small particles. This work contains an examination of the feasibility of characterization of a small particle through a simple scalar diffraction setup. Chapter 5 focuses on the use of Fraunhofer diffraction theory for the measurement of stationary particles. The pattern styles observed are a single dot, an array of dots, and a single line. A laser beam passed around the samples and resulted in diffraction patterns. Various methods were used in order to investigate the sample characteristics.

After the ink has hit the substrate and the printed pattern has formed, a different diffraction system is proposed. This system uses a combination of lenses in order to recreate the sample image on the camera as opposed to the diffraction pattern from chapter 5. This sample pattern then goes through an image processing program which eliminates any background noise from the image and identifies the size and location of all of the dots. The distribution of the dots was then compared to measurements made using an optical

microscope, and the results are discussed. These methods are used for the measurement of the E-jet printing processes in this work but the methods are not limited to this additive manufacturing process.

The e-jet printing portion of the hybrid manufacturing has been introduced. The other component of this hybrid manufacturing system is a laser ablation setup. The goal of this hybrid setup is to use laser ablation to created grooves which are then filled using e-jet printing. As previously mentioned, various materials can be used as the substrate in the e-jet printing process. For this purpose, the interaction between various materials, mainly polymers, need to be investigated. Chapter 2 contains a literature review on the most commonly used polymers in laser ablation and their relationship with various types of laser. With this review, the readers should have a general understanding of the trends that are present in laser ablation.

All of this investigation represents the groundwork for the creation of a hybrid system. Various inspection methods have been proposed, many of which are capable of in-process measurements. As of now, there are not any in-process inspection methods which are used in e-jet printing. In addition, the work described in chapter 5 may also be able to characterize the quality of laser ablated grooves, but this will be discussed more in the future outlook.

CHAPTER 2. LASER ABLATION OF POLYMERS: A REVIEW

Modified from a manuscript published in Polymer International

Sandeep Ravi-Kumar[a], Benjamin Lies[a], Xiao Zhang[a], Hao Lyu[b], Hantang Qin[a]

[a]Industrial and Manufacturing Systems Engineering, Iowa State University, Ames, IA 50011 USA; [b]College of Mathematics and Physics, Qingdao University of Science & Technology, Shandong, China

Abstract

Laser Ablation (LA), which employs a pulsed laser to remove materials from a substrate for generating micro/nano structures, has tremendous applications in the fabrication of metals, ceramics, glasses, and polymers. It has become a noteworthy approach to achieve different functional structures in engineering, chemistry, biological, medical and other fields. Polymers are one such class of materials, they can be melted and vaporized at high temperature during the ablation process. A number of polymers have been researched as candidate substrates in LA, and many different structures and patterns have been realized by this method. The current states of research and progress were reviewed from basic concept to optimal parameters, polymer types and applications. The significance of this paper is to provide a basis for follow-up research that leads to the development of superior materials and high-quality production through LA. In this review, we first introduced the basic concept of LA, including mechanism, laser types (millisecond, microsecond, nanosecond, picosecond, and femtosecond) and influential parameters (wavelength, repetition rate, fluence, and pulse duration). Then, we focused on several commonly used polymer materials (PTFE, PI, PDMS, PET, and PMMA) and compared them in detail, including the effects of polymer properties,

laser parameters, and feature designs. Finally, we summarized the applications of various structures fabricated by LA in different areas along with a proposition of the challenges in this research area. Overall, a thorough review of laser ablation on several polymers has been presented, which could pave the way for characterization of future novel materials. This is to be used in the future in combination with along with E-jet printing to form a hybrid system.

Introduction

The laser is the acronym for “light amplification by stimulated emission of radiation”, typically a high-intensity beam of electromagnetic radiation. The initial idea of laser theory was presented by Einstein [1]. However, the first ruby laser was developed in the year 1960 by the physicist Theodore H. Maiman. Soon after the experimental realization of the laser, there were several practical applications such as in the military, health, industrial and scientific fields. The first widely recognized application were laser printers, which were invented in 1971 by an American engineer Gary Starkweather [2]. There are significant applications of laser in manufacturing sectors like laser drilling [3], laser cutting, holography, laser metal deposition and laser additive manufacturing [4, 5].

Conventional machining techniques such as drilling, welding, milling, and turning are all capable of machining a wide variety of materials. However, it is difficult to achieve the best results in terms of surface finish and aspect ratio in machining hard-to-machine materials such as titanium [6] and super alloys [5]. The requirements of these industries led to the development of novel machining processes such as laser beam milling [7, 8], laser drilling [3], and laser etching [8, 9]. All of these laser involved machining operations share a common phenomenon known as laser ablation.

Laser ablation is the top-down process of removing material by focusing a laser beam onto a substrate. Ablation occurs only when the material absorbs sufficient energy to be melted or vaporized. The history of laser ablation began with the discovery of the ruby laser in 1960. Following its discovery, several researchers proposed works describing the fundamental elements of ablation. In 1962, Breech and Cross collected and spectrally dispersed the light emitted from the ablated metals [10]. This formed the basis for the laser microprobe emission spectroscopy technique used for elemental analysis of solid materials. Linlor in 1963 used time of flight measurements to determine the energy possessed by the ejected ions during ablation [11]. The first observation of photoemission of electrons was in the year 1963 by J.J Muray [12]. Other notable milestones in the history of laser ablation were the first study of ablation of biological material by Rosan in the year 1963 [13], and the observation of laser ablated carbon, boron, and manganese clusters by Berkowitz in 1964 [14]. The first instance of using laser ablation for deposition of thin films was reported in 1965 by Smith [15]. The rest of the sixties saw the expansion of the previous studies over numerous other targets. Studies were focussed on an extensive array of laser characteristics such as the wavelength, pulse duration, power etc. Since then, the development and understanding of laser ablation have been incremental.

Laser ablation is widely used in the fabrication of metals, ceramics, glasses, and polymers. Polymers are of great interest due to unique properties such as light weight, corrosion resistance, lower frictional properties, less wear in comparison to metals [16] and its application potentials. In recent years, polymer-based laser ablation has gained huge interests due to its ability to fabricate microfluidic channels [17], optical waveguides [18], and flexible electronics. The first report on the laser ablation of polymers was by Cozzens

1977 [19]. He used an infrared laser source (λ=10.6μm) to irradiate eleven different polymers. Since then, there has been a rapid rise in the applications of polymers such as nozzles for inkjet printers [20] and multi-chip modules [21]. Consequently, researchers started exploring the various aspects of using laser ablation for processing polymeric materials for such applications. For instance, researchers studied the influence of laser type and parameters on the accuracy and precision of the ablated features on the polymer materials. In this paper, different laser types (see table 1) and the influences of laser parameters on ablated structures were reviewed. Furthermore, we reviewed several common polymer materials used for laser ablation including Polytetrafluoroethylene (PTFE), Polyimide (PI), Polydimethylsiloxane (PDMS), Polyethylene Terephthalate (PET) and Polymethyl Methacrylate (PMMA). The feature structures, laser dependence, and properties were compared among those polymers. The review of laser ablation was based on the research activities of various groups, which can show the general development of this manufacturing method and provide an outlook that may pave the way for further development and application of laser ablation.

The organization for the remainder of this paper was as follows. First, the laser ablation process was reviewed in Section 2. Then, the current state-of-the-art laser ablation on various polymers was discussed in Section 3. Finally, different applications, challenges, and future scopes were summarized.

Laser Ablation

Mechanisms of Laser Ablation

The general mechanism of laser ablation is consistent throughout laser machining applications such as laser beam milling, high-precision drilling, and laser cutting. Ablation is

a combination of both vaporization and melt expulsion as represented in Fig. 1. When a focused beam of laser radiation strikes a surface, the electrons present in the substrate are excited by laser photons [22]. This excitation results in the generation of heat by absorbing photon energy, which is consistent with Beer Lambert's law [22, 23]. Beer Lambert's law states that the amount of light absorbed is dependent on the thickness of the materials and intensities of the light source. The heating effects cause melting or vaporization of the material, thus resulting in the removal of macroscopic materials from the substrate. The transition from solid to gas results in the formation of a plasma plume.

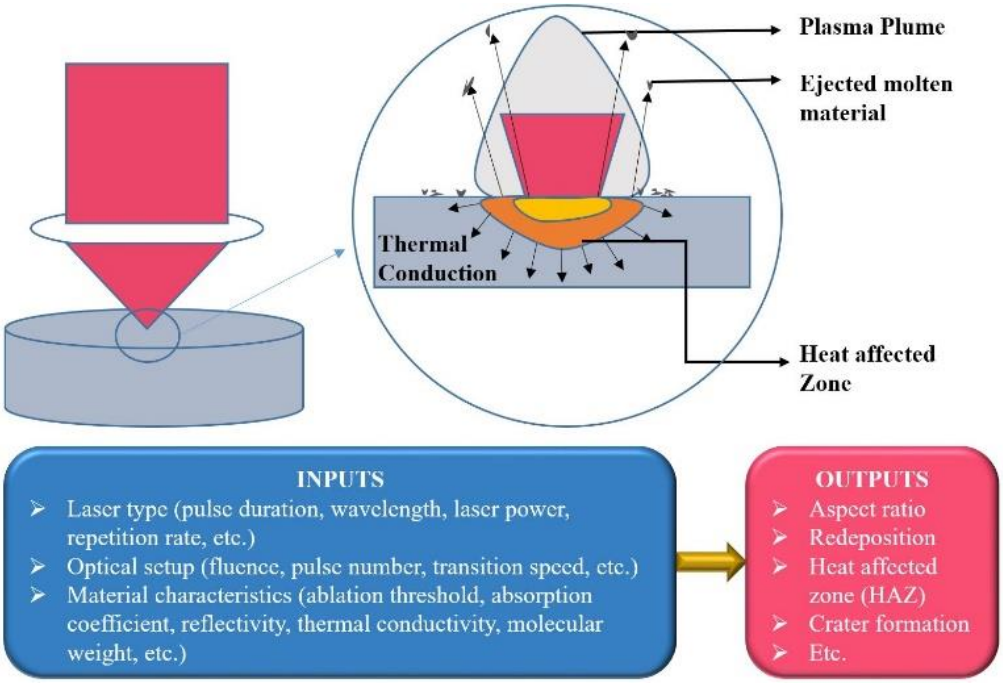

Figure. 1. The mechanism at the laser-material interface.

This phase transition takes place in a series of steps. The initial heat produced by the absorption of the laser photons results in the formation of a melt pool at the laser-substrate interaction zone. The temperature further increases due to the incoming pulses and the melt pool reaches the vaporization state [24]. High pressure is created during vaporization, which is also called a recoil pressure, which pushes molten materials from the pool where it is

ejected [25]. The ejected material is a concern due to its redeposition on the substrate or on the interaction zone [26, 27]. By further increasing the temperature at the laser-substrate interaction zone, the liquid attains an explosive liquid vapor phase transition stage [28, 29]. The above mechanism is commonly seen during ablation using long pulsed lasers and is may be referred to as a “burst”. In this mechanism, the dynamics of the fluid phase and the vapor conditions are quite complex and the resolidification of the molten material also results in geometric changes in the ablated features.

Based on properties of the laser and material such as fluence, absorption coefficient, reflectivity, wavelength, and pulse duration, the ablation mechanism can be purely chemical, thermal, or a combination of both. Photochemical ablation occurs due to the breaking of the covalent bonds in the polymer chains via the energy of the UV photons. Photothermal ablation considers the electronic excitation by the UV photons to be thermalized which then results in the breaking of the polymer bonds. Several researches have focused on explaining the mechanisms present at the laser-material interaction area by assuming one mechanism dominates and then simulating the dominant process [30-32]. Hu [33] used femtosecond laser pulses to generate microscopic phase transformation on the graphite surface, and obtained melted part in the edge area of gentle ablation. A cavity microball lens was fabricated by Chen [34] with a femtosecond laser, and they also proposed a heat diffusion model to help better understand the laser-material interaction. These various mechanisms are all dependent on the specific combination of light and material properties. As a result, it is essential to consider certain important phenomena while studying the laser-material interaction. These phenomena include the type and magnitude of light energy absorption and the time scale of the laser pulse. The extreme intensity of the laser pulse in the ultrashort time frame provides

inaccurate predictions under classical heat transfer conditions. At normal intensities, the absorption is linear and follows Beer Lambert's law. This implies that the electrons excited due to the photon absorption transfer the heat to the lattice, thereby resulting in melting and vaporization. However, at ultrashort timescale, the absorption becomes nonlinear and becomes intensity dependent. The bound electrons of the material can be directly ionized by the large absorption coefficient and due to high-intensities. Therefore, it is essential to characterize the laser being used and to predict the mechanism occurring at the laser-material interaction zone. These various mechanisms are all dependent on the specific combination of light and material properties. In practice, there are limitations regarding which combinations can be achieved, which is explained in the following sections.

Ablation Parameters

In order to better study polymer laser ablation, it is essential to understand the parameters involved. Laser ablation of polymers depends on a variety of factors such as laser wavelength [35, 36], repetition rate [37], fluence [38], and pulse duration [39]. Firstly, for a laser system, two characteristics are important to laser ablation, the monochromaticity, and directionality of the beam. The monochromaticity means that the wavelength of all emitted light is the same. This singular wavelength is very useful for calculations regarding the interaction of the light with optical components and material. The directionality of the beam refers to a low angle of divergence, this increases the ease at which the light is controlled and focused. The effective optical spot size, directly related to laser fluence, is different for each system and plays a very important role in ablation. Here, the fluence is the total energy of the laser over the area represented by the focal spot size and is typically measured in J/cm2. The most common laser type used in the ablation process is the pulsed laser. Pulsed lasers have a higher peak power than continuous beam lasers. This is useful as the energy doesn't surpass

the ablation threshold is absorbed into the material. The excess energy results in a larger heat affected zone, which lowers the quality of the material.

In the case of pulsed lasers, it is appropriate to measure the fluence of each pulse as opposed to the fluence over the total time. These individual pulses can vary in duration and in repetition rate and are characteristic of the laser type, which will be discussed in the next section. The positioning of the focal spot of the laser on the substrate influences the etch rate, redeposition of the debris and the microstructures formed on the sample surface [40]. The research conducted by Wang reported easier machining and lesser debris redeposition while focusing the laser near the bottom surface of the sample [41]. Lei studied the backside and front side ablation of gold film on a silicon substrate under varying pulse energies and focal positions F[42]. He accounted for the presence of two types of damage happening based on the laser fluence: Ablation and Burst. He used Finite Element Modeling simulation to verify the burst damage occurring during the back-side ablation.

In addition to the influence of the laser source, properties of the substrate materials such as thermal conductivity [43], absorption coefficient [44] and reflectance [45] have all been observed to influence the ablated structures as well. Regardless of the fluence of an incident laser, absorption of photons by the material is essential for ablation to happen. Each material has unique absorption coefficients for different wavelengths. For example, polymers generally exhibit increased absorption of the photons at ultraviolet wavelengths. Once the light has been absorbed by the material, it is important to consider how the surrounding material is affected by the transfer of heat through thermal conductivity. The molecular weight of the polymer also influences the ablation efficiency [46]. It has been reported that

the increase in molecular weight results in a highly viscous molten material during ablation and consequently results in lower ablation rate of the polymer [47].

The combination of these material characteristics and the optical properties of the incident light resulting in various ablation mechanisms. The emphasis on which mechanism to focus on is dependent on the application of the light/material interaction. The focus of this review is laser ablation of polymers, all of which emphasize the same general mechanism. The ideal output characteristics of these mechanisms include high aspect ratios, limited heat affected zone, minimal material redeposition, and better minimum resolution on polymers.

Laser Source

The laser sources can be classified based on their wavelengths into ultraviolet/excimer lasers and infra-red lasers. An excimer laser is a pulsed gas laser that emits UV light with a power efficiency between 0.2% and 2% [47]. Excimer lasers gained attraction because most polymers exhibit high absorption coefficient at excimer wavelengths and the ease at which the laser can be focused onto the work surface using an aperture [48]. Typical examples of excimer lasers are F2, ArF, KrF, XeCl, and CeBr lasers having an emission wavelength in the ultraviolet spectrum (10 to 400 nm) [47]. A drawback of using excimer lasers for ablation purpose is that the gas used as the laser medium has to be changed more frequently. As a substitute for these excimer lasers, diode pumped solid state lasers such as Nd: YAG laser was used [49, 50]. They are capable of achieving the ablation threshold at small spot sizes because of high-quality beams but it is difficult to mask the laser without forming diffraction patterns on the irradiated surface. In addition to UV lasers, infra-red lasers have also been used in ablating materials. For, instance, Infrared laser has been used in ablating PMMA, PTFE, and PI materials [19]. However, unlike UV wavelengths, polymers do not exhibit excellent photon absorption in the infrared wavelengths.

Table 1. Types of polymer ablated corresponding to different laser sources

Polymer	**Laser Sources**
Polymethyl Methacrylate (PMMA)	KrF laser[53-56], Nd: YAG laser [57], ArF [55, 58, 59], KrCl [55], XeCl [46, 60], CO_2 [46]
Polystyrene (PS)	KrF laser [53], ArF laser [61, 62]
Poly(α-methyl styrene)	ArF [59]
Polyimide (PI)	XeCl [63-68], ArF laser [19, 67-69], KrF laser [70, 71], XeF laser [69], Nd: YAG laser [72, 73], KrCl laser [65], Nd: YVO_4 [74]
Polyethylene Terephthalate (PET)	ArF laser [59, 75], KrF laser [53], XeCl [64]
Bisphenol Polycarbonate (BP PC)	ArF laser [59], KrF laser [53, 76]
Polyethylene (PE)	Iodine PALS [77]
Polytetrafluoroethylene (PTFE)	KrF laser [53, 78]
Polyether Ether Ketone (PEEK)	XeCl laser [79], KrF laser [80], Nd:YAG [81], Nd:YVO_4 [82, 83], CO_2 [84]
Polyacetylene	ArF laser [74]
Polydimethyl Glutaramide (PMGI)	XeCl laser [46, 85]
Polyetherimide (PEI)	ArF laser [86], XeCl laser [86], KrF laser [86], Nd:YAG [87]
Nylon	XeCl laser [88], Nd:YAG [88, 89], CO_2 [88]
Polydimethylsiloxane (PDMS)	CO_2 laser [90, 91], Ti:sapphire laser [92], ArF laser [93], Erbium doped fiber laser [94]

The other way to classify laser sources is based on the timescale of their pulse durations. The lasers are classified into millisecond (ms, 10-3s), microsecond (μs, 10-6s), nanosecond (ns, 10−9s), picosecond (ps, 10-12s), and femtosecond (fs, 10-15s) lasers. The timescale of the laser pulse duration influences the ablation mechanism, accuracy, and precision of the features. Millisecond and microsecond lasers are produced by chopping the continuous wave laser beam. It has been reported that the ablation of polymers by long pulses, leaves evidence of molten materials and carbonization of the walls of the ablated

features [51]. Unlike longer laser pulses, ultrashort laser pulses in the timescales of femtoseconds or picoseconds provide advantages in terms of high precision, large material removal rate, and minimal thermal damage. It is attributed to two processes: thermal diffusion and nonlinear absorption. In the ultrashort timescale, there is insufficient time to transfer the heat energy from the excited electrons to the lattice, causing minimal thermal damage. However, under extreme intensities, the plasma plume generated tends to result in heating of the surrounding material. This minimization in energy loss due to thermal diffusion helps achieve features with high aspect ratios, no recast layer and minimal cracking [52]. Each individual laser setup is limited to a specific range in regards to wavelength and pulse duration. This is a major limiting factor that needs to be considered prior to any proposed experiment.

Polymer Materials

Laser parameters and material properties both affect the success of laser ablation. Aside from researches on the creation of the laser beams, the materials themselves have been heavily studied. Research has been conducted on polymer materials that have promising applications in various fields such as medical, engineering, and chemical sensing. The materials required of these fields limit the composition and thus the material characteristics that are integral to performing laser ablation.

The polymers used for laser ablation have been classified based on several criteria such as their availability, application, ablation behavior, and decomposition behavior. For example, Polymethyl Methacrylate (PMMA) depolymerizes upon irradiation while polyimides (PI) decompose into fragments upon irradiation. Similarly, certain polymers are available readily such as PMMA, PET, and PTFE, whereas some are customized based on

specific requirements of the application (Designed Polymers). Certain polymers such as PDMS and Polycaprolactone are used in biomedical applications such as venal implants and cell encapsulation. A summary of polymers and related laser sources are listed in Table 1.

Polytetrafluoroethylene (PTFE)

Polytetrafluoroethylene (PTFE), also known as Teflon, is a crystalline synthetic fluoropolymer of tetrafluoroethylene. Teflon, with an absorption coefficient, is a weak absorber. It is a highly versatile material used in a wide variety of applications owing to its stability and durable characteristics. Due to its good electrical resistance, it is used as an insulator for wiring and cables. PTFE is used in mechanical engineering applications in parts that have sliding action such as gears and pulleys since they have a low frictional coefficient. PTFE is widely used in the food packaging industry and in the chemical industry as a material for sealing aggressive chemicals. As mentioned previously, each application requires different material characteristics. This leads to the creation of several grades of PTFE based on the filler material incorporated into it. Venkateshwarlu studied the effects of various fillers on the mechanical properties of PTFE based composites [95]. He used glass, bronze, carbon, mica, sand, porcelain, alumina, antimony trisulphide and marble as fillers and studied the mechanical properties including hardness and tensile strength.

With the versatility in the properties of PTFE for different grades, PTFE has been successfully applied in the medical and the electronics sector. For example, membranes of PTFE are used as a barrier for bone promotion around titanium implants [96]. These applications involve the material to have features in micro/nano scale and demand precision. Researchers investigated the methods to minimize defects such as heat affected zone and surface dendrite formation. Kuper studied the ablation of PTFE with femtosecond UV laser

pulses at 248 nm [53]. He reported that thermal damage was absent for fluences as low as 0.5 J/cm2 with an ablation rate of 1 μm per pulse.

Womack studied the use of femtosecond laser ablation in depositing thin films of PTFE on silicon wafers [78]. She emphasized that the femtosecond (fs) lasers produced precisely machined features, unlike nanosecond laser pulses. The deposition rate and film quality were characterized by using scanning electron microscopy, x-ray diffraction, and IR spectroscopy, which showed strong supports of high deposition and quality by using fs laser pulses. Huber studied the ablation rate of sintered PTFE and reported its dependence on the wavelength of the laser [97]. He reported that, at a given laser fluence value, the ablation rate increased initially and then decreased as the wavelength increased. He further stated that there was no relation between the experimentally measured ablation depth and the linear optical penetration depth, which was calculated using a Monte Carlo simulation. Mitra measured the laser ablation threshold of PTFE using a photo thermal beam deflection technique [96]. He measured ablation threshold at different wavelengths and estimated the coefficient of absorption of Teflon at each wavelength. He reported that the value of the absorption coefficient increases with a decrease in wavelength. Wang investigated laser ablation of PTFE in ambient air [98]. He reported the clear edge definition and increase in ablation depth can be achieved by increasing the number of pulses. The effect of air ionization at higher fluences in deteriorating the ablated structure quality and decreasing the ablation efficiency were reported. While all other researches were focused on ablating pure PTFE, there have been researches who focused on identifying the advantage of doping PTFE. Yang reported the ablation of PTFE doped with aluminum nanoparticles [99]. He reported

that the doped Teflon can be ablated precisely using near infra-red lasers and does not require a vacuum ultraviolet or femtosecond excimer laser.

Polyimide (PI)

Polyimide is a high temperature engineering plastic. Polyimides are thermally stable even up to the temperature range of 300-400 ˚C. As a result of its high heat and fire resistance compared to other polymer materials, PI is suitable for a diverse range of applications such as aerospace, opto-electronics, and defense. They have good machinability, electrical and thermal insulation properties [100].

The machining efficiency and etching mechanism of polyimides via laser ablation have been investigated. Brannon studied etching of polyimide using pulsed excimer lasers of different wavelengths (248, 308, 351 nm) [63]. He reported that the laser ablation threshold at which significant etching occurred can be correlated with the wavelength dependent absorption coefficient. It was stated that the absorbed energy per unit volume required to etch the substrate is equal for several distinct wavelengths. It is reported that the presence of oxygen does not influence the etch rate, but it controls the oxidation of the ablated material. Yu, Ma, and Lei conducted laser ablation of molybdenum (Mo) on the polyimide substrate using the axicon lens [101]. They studied the narrow grooves produced by ablation under varying parameters such as laser power, scanning speed and the axicon tip distance from the sample. Selective scribing of the Mo material on the PI substrate was attributed to the large difference in threshold fluence of Mo and PI (0.18J/cm2 and 0.75J/cm2 respectively at 60 fs pulse duration). They reported that the use of an axicon focused beam could produce narrow groves of high quality even with large height fluctuations of moving substrates. Sturesson [102] used YAG laser for thermotherapy to investigate the coagulated lesions produced using

a cylindrical diffuser and found carbonization phenomenon at the metal-covered tip both experimentally and theoretically.

Research has been conducted to determine the influence of laser parameters such as pulse duration and pulse repetition rate on the ablation of polyimides. Taylor used photoacoustic spectroscopy to determine the dependence of pulse duration on ablation of polyimide using a XeCl laser source [64]. He ablated PI with a XeCl laser of pulse duration 7-300 ns and reported that the ablation threshold has a weak relation with the pulse duration. He observed an etch depth of 0.1-1 μm per laser pulse and it was independent of the pulse duration. However, there are other processes that occur during laser ablation of PI at particular pulse durations. Chuang studied the laser ablation of PI using an Nd: YAG laser (355 nm) in order to investigate the saturation of ablation rate with an increase in laser fluence [72]. He reported 80 percent saturation at the fluence of 0.5 mJ/cm2. He measured the reflectivity, emission intensity and photoacoustic signal based on the fluence values. It was concluded that the trailing part of the laser pulse was blocked by the plasma plume and the excited polymer particles, which prevented the laser from hitting the polymer substrate.

Apart from saturating the ablation rate, the debris formed has been found to have an influence on the morphology of the ablated polymers. Taylor studied the distribution of the ablated debris formed during the XeCl laser (308 nm) ablation of pure and dopant induced PI [65]. Similar to Dyer [103] and Niino [104], Taylor observed cone like structure formation on the surface of both polymers. He reported that the cone formation was due to the redeposition of the debris and not based on impurities in the polymer.

Polydimethylsiloxane (PDMS)

PDMS is a mineral-organic polymer belonging to the siloxane family. The structure of the PDMS consists of carbon and silicon. PDMS has been widely used in the fabrication

of microfluidic devices. It is used as a food additive as and an anti-foaming agent in beverages. One reason to use PDMS to manufacture microfluidic devices is its transparency at optical frequencies which allows for visibility of the contents in the micro-channel. Additional reasons include its auto fluorescence [105], biocompatibility and inexpensiveness compared to the previously used materials such as silicon.

Researchers studied the use of laser ablation with PDMS to manufacture microfluidic devices of different features in a cost-efficient manner. Yan studied the use of laser ablation technique to produce single layer microfluidic devices with abrupt depth variations [90]. He used the laser to engrave channel patterns on to PMMA plate and then used it to create the master pattern for the single layer PDMS microfluidic devices. He reported the capability of this technique to produce microfluidic devices with micrometer structures in one step. Li reported a simple cost-effective method for fabricating microfluidic devices with PDMS multilayer configurations [91]. He used a system similar to Yan and used conventional lithography, and sputtering technique to fabricate an alignment bonding of top and bottom electrode patterned substrates. This was used for integration of the electronics in the microfluidic devices. He further validated the proposed method by fabricating and testing a dielectrophoresis based integrated electronic microfluidic chip for the manipulation of micro particles. Wolfe studied Ti: sapphire laser (femtosecond pulses) production of stamps for micro contact printing and for the fabrication of microfluidic channels [92]. This proposed technique was capable of producing features as small as 1 μm in width and 2 μm in pitch. Unlike conventional molding, this technique does not need curing.

Unlike using a mask for fabricating the PDMS micro-channels, researchers focused on identifying methods for direct fabrication of the microchannels on polymer materials.

Hautefille reported a technique to etch microscale volumes of material from PDMS surface [106]. He utilized infra-red laser along with microscopic clusters of carbon materials to generate micro plasma at the PDMS-air interface layer. Further, he reported the technique's application to fabricate interesting photonic features and the presence of combustion residues in the form of carbon nano domains with local fluorescence and increased hydrophobicity. Hsieh studied the direct micromachining of microfluidic channels on PDMS and other biodegradable materials such as polyglycerol sebacate [93]. He proposed a polymer surface modification method for fabrication of a microfluidic system, which eliminated the steps of mask/mold production as in photolithographic or soft photolithographic technique. He also investigated the relationship between laser parameters, depth and width of the ablated features.

Another research topic in the field of laser ablation of PDMS is direct micropatterning and fabrication. Huang studied the thin layer separation and micro-fabrication of PDMS using an ultrashort pulsed, IR laser (1552 nm) [94]. The influence of pulse overlap rate and irradiation pulse energy on the ablation width, depth and surface quality are analyzed. He reported a pulse overlap rate range of 1-2 pulses per μm and 1-1.5 μJ to achieve quality separation and fabrication without any visible thermal damages. Moon studied the effect of crater size on the surface morphology of PDMS [107]. He studied the PDMS surface with varying both the interpulse interval and the inter-spot distance between successive pulses. It was reported that the surface morphology was dependent both on the inter-spot distant and interpulse interval between successive pulses.

Polyethylene Terephthalate (PET)

PET is a commonly used transparent thermoplastic in the textile industry as polyester, packaging industry, and as an engineering plastic when combined with other materials such

as glass fiber to improve the material strength. There have been numerous studies on the application of laser ablation for micromachining of PET and the mechanism occurring at the laser-material interaction zone. Watanabe studied the fragmentation of PET during laser ablation using 248 nm excimer pulse to characterize the ablation mechanism [89]. He reported that the fragmentation was accelerated by thermal energy at fluence above the threshold value of 30 mJ/cm2. He stated the importance of both thermal and photochemical reactions in the ablation of PET. Other defects observed during the laser ablation of PET are studied by investigating the surface of the substrate. Arenholz studied the surface of PET after irradiation by an ultraviolet laser at various wavelengths (193 nm, 248 nm, 308 nm) to better understand the growth and structure of surface dendrites using atomic force microscopy [108]. He reported that the size (length of dendrite arms) and structure of the dendrite were dependent on the laser wavelength and the ambient pressure. By studying the surface of PET after ablating with a 193 nm ArF laser [75], Lazare reported an increase in surface roughness as the number of laser pulses increased. The surface roughness peaked at a maximum of 1-2 μm at 10 pulses.

There were researchers who tried to understand the contribution of laser ablation on the morphological changes in the material. Mansour studied the surface induced morphology changes on ablating PET using an Nd: YAG laser of 266 nm [109]. He proposed a theoretical model to determine the ablation etch depth for a given incident laser fluence. P.E. Dyer studied the excimer laser ablation of PET and reported the thermal coupling and etch rate measurements and observed that a thermal balance was present up to the threshold fluence and above which the ablated material removed excess energy [68].

The influence of laser parameters such as pulse width and wavelength on the ablation efficiency and surface morphology have been investigated. Liu studied the difference between the use of short and long pulses for the ablation process [110]. He used a Ti: sapphire laser source to ablate PET. He reported that the heat affected zone, cracks, and nonuniform ablation were more frequent during ablating with a higher pulse width (200 ps) as opposed to a shorter pulse (80 fs). With the increasing interests in identification of the cause of defects, researchers started to investigate methods to control defect growth during laser ablation. Elaboudi studied the photoablation of polymers under water and compared it with ablation in the air [111]. He reported that the threshold fluence decreases while ablating under water and aimed at identifying the hydrolysis reaction responsible for the decrease in laser threshold.

Polymethyl Methacrylate (PMMA)

PMMA is another type of low-cost thermoplastic also known as acrylic glass. It is widely used in applications such as optical, biomedical, solar, sensors and nanotechnology. There have been numerous studies geared toward understanding the application of ablation for machining PMMA. Specifically, how the precision and resolution (aspect ratio, recast layer, redeposition, micro-cracks) are affected by the laser as well as the material properties (absorption coefficient and thermal conductivity). Nayak studied the effects of laser power and processing speed on the precision of the depth, width and surface profiles of microchannels manufactured on PMMA of different polymer weights (96.7 kDa, 120 kDa, 350 kDa, and 996 kDa) using a CO2 laser [46]. He observed that the depth and width increase along with laser power. There were pores formed in higher molecular weight PMMA whereas none were observed in lower molecular weight samples. He reported that

the choice of material was the key factor for CO2 laser ablation for applications that require high precision.

Similarly, Baudach studied the precision of the width and depth of features machined on PMMA films of 250 μm using Ti: sapphire laser. He observed that the ablation threshold value varied between 0.5-2.5 J/cm2 depends on the number of laser pulses hitting the spot. He reported that the diameter of holes (μm) was influenced by the laser fluence and the number of pulses [112]. Beyond studying the precision of the machined features, researchers paid great attention to device fabrication and testing. Klank reported the ease of producing microfluidic channels in PMMA using a CO2 laser. He reports that the feature depth can be controlled by the laser power and scanning speed [113]. The Gaussian beam created during LA has been verified to help for self-aligning the optical fibers. Osellame [114] explored the physical and chemical property effect of the ablation of femtosecond laser on the surface of PMMA. Chen [115] fabricated microball lens in PMMA with the femtosecond fiber laser to realize the direct writing of micro lens inside transparent bulk polymer material, which has great application potentials in multi-function integrated microfluidic devices.

Although laser ablation, under proper control of parameters, is capable of producing micro/nano scale features with precision and accuracy, there are a considerable number of defects such as a recast layer, redeposition of debris and heat affected zone. Researchers have studied the ablated debris to understand better the photochemical reactions occurring and the process by which the debris is ejected and then redeposited. Danielzik [58, 60] and Estler [57] used quadrupole mass spectrometry to study the ablated particles. Estler studied the photochemical composition of the ablated particles and reported the change in the composition with varying wavelengths. Danielzik studied the velocity distribution of the

ablated PMMA particles and reported it to change between thermal velocity distribution and Non-Maxwellian velocity distribution depending on the laser fluence. Burrell [59] used x-ray photoelectron spectroscopy to study PMMA and Poly(α-methyl styrene) surface composition after irradiating it with a laser in the UV wavelength. He reported the absence of surface compositional changes, which indicated that no surface intermediates that are different from the starting material were formed.

Formation of craters around the ablated surface is another defect that has been investigated. Efthimiopoulos studied XeCl laser ablation of weakly absorbing PMMA and reported the formation and collapse of bubbles [116]. He stated that the phenomenon of bubble creation and collapse occur over multiple pulses while using 3-9 J/cm2 energy fluence. For high energy fluence (>9 J/cm2), the bubble creation and collapse occurs with single pulse duration. He concluded that successive pulses might be needed to advance the process of bubble creation and collapse based on the energy fluence.

There are other applications of PMMA such as thin film deposition and nanoparticle generation. Blanchet studied the deposition of thin films of PMMA by laser ablation using an Nd: YAG laser in the ultraviolet wavelength range [117]. He reported that the temperature of the substrate was important to determine the morphology and molecular weight the films. The films were maintained at temperatures between 100 and 200 ˚C. The deposition occurred due to the ejected monomer falling on the glass substrate and redeposited due to repolymerization of the monomers.

Other Polymers

Several other polymers have been studied for laser ablation. Polyetherimide (PEI), a high temperature resistant thermoplastic, is used for the production of PEI embossing tools. These tools are used for the packaging of membranes and production of microchannels for

the use of sealing bosses [87]. It was reported that the boss width was dependent on the laser diameter. Jensen studied the use of laser ablation for rapid prototyping of microsystems made of polymers [80]. He created a microsystem using Polyether ether ketone (PEEK), which can be used for injection molding a series of prototypes. He stated that this application could be extended to other thermally and mechanically strong polymers such as PEI. Natural polymers were studied by the ablation of a laser as well. Hu [118] fabricated a transparent and flexible carbon fiber net by heat treatment method, which provided a simple fabrication process with easy control of the size of the supercapacitor device.

Polyethersulfone (PES) is another polymer which has been widely used as a replacement for metals in automotive components. Similar to other polymers, researchers studied the mechanism that leads to the formation of these micro defects on the surface of the films. Laser induced surface microstructure formation was first reported by Dyer [103]. Niino observed the formation of microstructures on the surface of PES films while ablating with a XeCl laser source [104]. He studied the mechanism resulting in the formation of these microstructures using a XeF laser source. He reported that the thermal processes on the ablated surface played a significant role in the formation of the microstructures.

Although laser ablation of polymers was first reported in 1965, it was not possible to fully exploit the potential of polymer laser ablation using the commercially available polymers such as PMMA, PI, PTFE, PET, PEI, PES, PE, and PDMS. This was because of the drawbacks of these polymers such as carbonization, ablation debris redeposition and low sensitivity to laser radiation. This led to the idea of designed polymers: synthesizing polymers based on specific requirements of applications. The basic idea behind this approach is to combine the properties of one polymer with other. For example, Triazene polymers tend

to have high etch rates and good ablation quality but poor stability (oxidation of the substrate during irradiation). On the other hand, Polyesters exhibited higher stabilities but poor sensitivities (absorption at particular wavelengths). A designed polymer aimed at combining these two polymers in order to achieve high-quality machining (high surface finish, less heat affected zone, and high aspect ratio).

Similar to other commercially available polymers, researches have been conducted to understand the ablation mechanism, their efficiency and the defects that arise during their application. The impact of structural parameters on the ablation behavior and characteristics has been studied. Triazo based polymers are one class of designed polymers that contain triazene chromophore in its polymer chain. Lippert studied the laser ablation of triazene polymers films (50 μm thick) using PI as a reference polymer [119]. He measured the etch rates, threshold fluence and the surface defects induced during laser ablation. He reported that the polymers containing the triazene group have the lowest ablation threshold fluence (25 mJ/cm2) and the highest etch rate (3 μm/pulse). Lippert further investigated the triazene group polymer's laser ablation to identify the influence of etch depth per pulse on the laser fluence [120]. The complete absence of debris was attributed to the photolysis reaction that decomposes the fragments. It was concluded that the removal of material from areas larger than the laser beam was due to the generation of shock waves while irradiated with high-fluence laser pulses.

The dynamic behavior of the etching process was also investigated. Hauer studied the ablation of triazene group polymers and PI reference films using XeCl (308 nm) and ArF lasers (193nm) using nanosecond interferometry and shadowgraphy [121]. Similar to Lippert [119], he reported the absence of surface swelling and the presence of a shock wave. He

reported the etching of triazene polymer to start and stops with the laser beam. The speed of shock waves to increase with increasing influence and was higher for 193 nm than 308 nm wavelength laser beams.

Another class of designed polymers is the diazo based polymers. They exhibit excellent absorption at 308 nm wavelengths. Similar to triazo based polymers, these polymers contain a diazo chromophore in its polymer chain. Some of the examples of diazo based polymers are diazo sulfide polymer, diazo sulfonate polymer, and diazo phosphonate polymer. Jeffers studied the use of diazo coating in the preparation of printing plates by irradiating with laser light [121]. Busman invented a process of laser induced mass transfer imaging of materials using diazo compounds [122]. He emphasized that the new method improved the sensitivity of the laser induced thermal imaging through the use of diazo compounds.

Applications of Laser Ablation of Polymers

The application of laser ablation on polymers extends over a broad spectrum. The phenomena of laser ablation have been used in the LIGA process, which is a combination of lithography, electroplating, and molding. This process is typically used to create a pattern, which is then used for mass fabrication. The most commonly used polymer in the LIGA process is PI [123]. PI is coated over the silicon wafer substrate where laser ablation is then utilized to create micro features with high aspect ratios on the polymer material. Once the features have been formed on the polymer, electroplating is done to coat the polymer surface with metals [123]. Subsequent to the metal deposition, the polymer material can be dissolved resulting in the shell created by the metal coating. Because of PI's high thermal stability and insolubility in most solvents, there is difficulty removing it after electroplating. Current

research in this field is aimed at developing novel polymer materials that can meet the requirements of laser LIGA process.

Another widely used application of laser ablation is in the field of telecommunication. Fiber Bragg gratings (FBG) in the telecommunication field requires the outer layer of polymer material be removed in addition to the actual “inscription” on the fiber optics when obtaining side written gratings [124]. Some of the traditional ways of achieving this are by means of mechanical stripping or chemical stripping. However, there are disadvantages of using these techniques such as structural damages and environmental effects. Laser ablation for removal of the material has been found to overcome the limitations of traditional methods [125]. Further, researchers are investigating laser ablation for jacket striping of single mode fiber (SMF), which has a dual polymer layer system [126].

Laser ablation of polymeric materials has been extensively used in the fabrication of high performance photonic devices, micro fluidic devices, and optical waveguides. It has been reported that laser ablation can produce clean vertical cuts through plastics and polymer waveguide core [127]. This technique has been found to provide efficient coupling of light from optical fibers into polymer photonic devices. One example is the fabrication of micro lenses. A KrF excimer laser was scanned over successive contours of chosen diameter and scanning velocity. An array of the lens was fabricated based on the aperture used for shaping the laser beam. Naessens reported the method for micro lenses fabrication in polycarbonate material using an excimer laser [128]. Pan reported laser ablation of PI for the fabrication of polymeric micro optical components [129]. This method of fabrication of micro lenses provides flexibility in terms of shape, focal length, and diameter of the lenses.

The field of micro electro-mechanical systems (MEMS) have also adopted laser ablation. Lan reported the fabrication of MEMS on silicon and PI substrate by laser ablation using a 355 nm laser source [130]. He was able to manufacture microscopic holes and nozzles of various diameters using low power laser direct drilling. This fabrication technique is fast and clean compared to a traditional photolithography process. Hu [131] used dual-beam direct laser writing to fabricate a highly sensitive sensor of flexible polyimide sheets to detect femtomolar level detection of bisphenol A (BPA). The porous and conducting sensor can be applied for recovery analysis of BPA spiked in surface water.

Laser ablation has been used in the medical field for fabrication of biomedical devices for the use in minimally invasive surgery and other advanced surgical techniques. Laser ablation and other micromachining techniques help achieve the complex and small feature sizes required in these devices. In addition to the fabrication tools and devices for surgical application, laser ablation is directly used for surgery of the cornea. Trokel reported the use of excimer laser for removal of the corneal tissues in cow eyes [132]. The laser-tissue interaction was photochemical in nature. He also told of the absence of thermal damage to the adjacent tissues.

Challenges and Future Scope

Although laser ablation of polymers has been researched for the past two decades, there are still several challenges that have yet to be addressed. For instance, there are several models and simulations that try to explain the ablation mechanism at the laser-material interaction zone that results in the etching of the material. These models tend to explain the physics phenomenon such as absorption, reflectivity, optical excitation, thermal and chemical reactions to refer to the ablation occurring at the laser-material interaction. However, it is

difficult for a systematic way to explain the ablation mechanism of these phenomena. Some models assume the ablation occurs purely due to thermal reactions occurring due to laser irradiation while other models suggest chemical reactions are dominant. A single model cannot explain the ablation in different materials because the mechanism of ablation depends on the type of laser and the materials properties. Future research is needed in studying the contribution of each physical phenomena in etching the material and investigating an optimal model that accurately explains the ablation mechanism from a system point of view.

Micro/nano manufacturing requires high quality control of the material, precision, accuracy, and process during laser ablation. Despite the extensive study on laser ablation of a variety of polymers and understanding the influence of laser parameters and material properties on the ablation, there are inaccuracies in machining a feature of desired dimensions. Currently, it is difficult to create a feature of the exact desired depth and width. This is because of phenomena such as heating of the substrate over subsequent pulses, plasma plume formation and etch debris interfering with the subsequent pulses. Presently, there is no perfectly accurate physical model that helps in determining the optimal parameter for synthesizing the desired feature dimension. Future research focusing on establishing a quantitative model which can improve the parameter settings (spot size, repetition rate, pulse duration, intensity) required to achieve the desired dimension will contribute to increasing the application of laser ablation to various fields.

Further research in studying laser ablation of composite polymer materials would be of great scope. The use of fiber reinforced composites has become more common due to the strength and light weight of the material. Along with the growing use of composites, the need for composite repair and machining is growing as well. Traditional machining processes have

trouble with fiber reinforced composites due to the abrasive nature of the combination. Ablation may have great potential in that area as it has been used in the past to ablate fused silica (glass fibers) and various polymers in the past.

Summary and Outlook

Laser ablation has become a powerful method in the fabrication of micro/nano structures on various polymers. The discussions provided in the previous sections are an overview of the works done in the field of laser ablation over the past two decades for polymer-based laser ablation. The effect of laser parameters on machining, their influence on the substrate's surface morphology and the various applications of laser ablation have been studied. These parameters are dependent on both the material composition as well as the laser characteristics. Different laser types and influences of laser parameters to ablated polymeric structures have been reviewed. Several common polymer materials including Polytetrafluoroethylene (PTFE), Polyimide (PI), Polyethylene Terephthalate (PET), Polydimethylsiloxane (PDMS) and Poly Methyl Methacrylate (PMMA) are analyzed in the effects of polymer properties, laser parameters, and feature designs. The review of laser ablation is based on the research activities of different groups and can show the general development of this manufacturing method.

Several overarching trends have been observed throughout this review. While these trends can be used for a preliminary understanding of laser ablation, a deeper understanding should be derived from the works being reviewed.

1) Smaller pulse duration results in more vaporization and less melting. Higher Melting can cause a large HAZ and redeposition due to expulsion, cracks and non-uniformity. Also, more vaporization results in the formation of a plasma plume which can

reduce the quality of the ablated features due to saturation. 2) The absorption coefficient of a given material varies for different wavelengths. This needs to be well characterized in order to make any accurate predictions. This means that the combination of laser type and material used are very important. 3) A high repetition rate may not leave enough time for the plasma to disperse during vaporization, thus reducing the effectiveness of successive pulses due to interference. 4) Higher molecular weight can result in lower ablation rates due to the formation of highly viscous molten material during ablation. 5) A larger thermal conductivity of a material can lead to a larger HAZ, specifically with longer pulse durations.

As the development of modern manufacturing based on laser ablation, the coming years will see the further development of LA towards a precise controlling technology with many applications beyond polymers. Quantitative verification and the modeling of laser ablation are quite complex and can always be further improved. In addition to the study of the mechanisms of ablation, the precision, accuracy and process control can also be improved from a manufacturing point of view. Future research into establishing a quantitative model which can suggest the parameter settings (spot size, repetition rate, pulse duration, intensity) required to achieve the desired dimension will increase the applicability of laser ablation in various fields.

References

1. Einstein A, Physikalische Zeitschrift 18: 121-128 (1917).

2. Townes CH, Garwin L and Lincoln T, A century of nature: twenty-one discoveries that changed science and the world, University of Chicago Press,Chicago 2003: 107-112 (2010).

3. Larsson IF, Method and apparatus for drilling holes by means of a focused laser beam. US Patent US3410979A (1968).

4. Akinlabi ET, Rasheedat MM and Stephen AA, Advanced Manufacturing Techniques Using Laser Material Processing, ed by Akinlabi ET. IGI Global, British, pp 11-24 (2016).

5. Bogue R, Assembly Automation 35(2): 161-165 (2015).

6. Kuttolamadom M, Jones J, Mears L, Kurfess T and Choragudi A, Investigation of the Machining of Titanium Components for Lightweight Vehicles. SAE Technical Paper 2010: https://doi.org/10.4271/2010-01-0022 [accessed 22 April 2019].

7. Dubey AK and Yadava V. International Journal of Machine Tools and Manufacture 486: 609-628 (2008).

8. Raymond S and Mueller JLF, Method of using laser to coat or etch substrate. US Patent US3364087A (1968).

9. Chovan S, Device for visually displaying luminous patterns, US Patent US4065865A (1975).

10. Breech F and Cross L, Applied Spectroscopy 16(59):1 (1962).

11. Linlor WI, Physiological Society 7(440): 1 (1962).

12. Muray JJ, Photoelectric Effect Induced by High Intensity Laser Light Beam from Quartz and Borosilicate Glass. http://inspirehep.net/record/57/files/slac-pub-0012 [accessed 22 April 2019].

13. Rosan RC, Healy MK and McNary WF, Science 142(3589): 236-237 (1963).

14. Berkowitz J and Chupka WA. The Journal of Chemical Physics 40(9): 2735-2736 (1964).

15. Smith HM and Turner AF, Applied Optics 4(1): 147-148 (1965).

16. National Research Council, Polymer science and engineering: the shifting research frontiers, National Academies Press, http://nap.edu/catalog/2307 [accessed 22 April 2019].

17. Becker H and Gärtner C. Electrophoresis 21(1): 12-26 (2000).

18. Van SG, Hendrickx N, Bosman E, Van EJ, Thienpont H and Van DP, IEEE Photonics Technology Letter 18(9): 1106-1108 (2006).

19. Cozzens RF and Fox RB, Polymer Engineering & Science 18(11): 900-904 (1978).

20. Aoki H, Laser processing method to form an ink jet nozzle plate, US Patent US5736999A (1994).

21. Patel RS and Thomas AW, Applications in Microelectronic and Optoelectronic Manufacturing II 2991: 217-224 (1997).

22. Brown MS and Arnold CB, Laser Precision Microfabrication 135: 91-120 (2010).

23. Ahmed N, Darwish S and Alahmari AM, Materials and Manufacturing Processes 31(9): 1121-1142 (2016).

24. Von der Linde D and Sokolowski-Tinten K, Applied Surface Science 154: 1-10 (2000).

25. Hoffman J, Journal of Physics D: Applied Physics 48(23): 235201 (2015).

26. Singh S, Argument M, Tsui YY and Fedosejevs R, Journal of Applied Physics 98(11): 113520 (2005).

27. Tangwarodomnukun V, Likhitangsuwat P, Tevinpibanphan O and Dumkum C, International Journal of Machine Tools and Manufacture 89: 14-28 (2015).

28. Miotello A and Kelly R, Applied Physics A 69(1): S67-73 (1999).

29. Bulgakova NM and Bulgakov AV, Applied Physics A 73(2): 199-208 (2001).

30. Cain SR, The Journal of Physical Chemistry 97(29): 7572-7577 (1993).

31. D'Couto GC and Babu SV, Journal of Applied Physics 76(5): 3052-3058 (1994).

32. Mahan GD, Cole HS, Liu YS and Philipp HR, Applied Physics Letters 53(24): 2377-2379 (1988).

33. Hu A, Rybachuk M, Lu QB and Duley WW, Applied Physics Letters 91(13): 131906 (2007).

34. Zheng C, Hu A, Kihm KD, Ma Q, Li R, Chen T and Duley WW, Small 11(25): 3007-3016 (2015).

35. LaHaye NL, Harilal SS, Diwakar PK, Hassanein A and Kulkarni P, Journal of applied physics 114(2): 023103 (2013).

36. Aguiar R, Trtik V, Sánchez F, Ferrater C and Varela M, Thin Solid Films 304(1-2): 225-228 (1997).

37. Burns FC and Cain SR, Journal of Physics D: Applied Physics 29(5):1349 (1996).

38. Okamuro K, Hashida M, Miyasaka Y, Ikuta Y, Tokita S and Sakabe S, Physical Review B 82(16):165417 (2010).

39. Chichkov BN, Momma C, Nolte S, Von Alvensleben F and Tünnermann A, Applied Physics A 63(2):109-115 (1996).

40. Wang W, Mei X, Jiang G, Lei S and Yang C, Applied Surface Science 255(5): 2303-2311 (2008).

41. Wang ZK, Seow WL, Wang XC and Zheng HY, Journal of Laser Applications 27(S2): S28004 (2015).

42. Lei S, Grojo D, Ma J, Yu X and Wu H, Procedia Manufacturing 5: 594-608 (2016).

43. Pham D, Tonge L, Cao J, Wright J, Papiernik M, Harvey E and Nicolau D, 11(5): 668 (2002).

44. Johnson SL, Schriver KE, Haglund Jr RF and Bubb DM, Journal of Applied Physics 105(2): 024901 (2009).

45. Benavides O, Golikov V and Lebedeva O, Applied Physics A 112(1): 113-7 (2013).

46. Nayak NC, Lam YC, Yue CY and Sinha AT, Journal of Micromechanics and Microengineering 18(9): 095020 (2008).

47. Paschotta R, Field guide to laser pulse generation, ed by Rudiger P. SPIE press, Bellingham, pp 23-26 (2008).

48. Speidell JL, Pulaski DP and Patel RS, IBM Journal of Research and Development 41(1.2): 143-148 (1997).

49. Chang WS, Shin B, Kim JG and Whang KH, Journal of Micro/Nanolithography, MEMS, and MOEMS 3(3): 472-478 (2004).

50. Dyer PE, Pervolaraki M and Lippert T, Applied Physics A 80(3): 529-536 (2005).

51. Nelson JS, Orenstein A, Liaw LH and Berns MW, Lasers in Surgery and Medicine 9(4): 362-374 (1989).

52. Srinivasan R, Hall RR, Loehle WD, Wilson WD and Allbee DC, Journal of Applied Physics 78(8): 4881-4887 (1995).

53. Shirk MD and Molian PA, Journal of Laser Applications 10(1): 18-28 (1998).

54. Küper S and Stuke M, Applied Physics B 44(4): 199-204 (1987).

55. Kawamura Y, Toyoda K and Namba S, Applied Physics Letters 40(5): 374-375 (1982).

56. Davis GM and Gower MC, Journal of Applied Physics 61(5): 2090-2092 (1987).

57. Dijkkamp D, Gozdz AS, Venkatesan T and Wu XD, Physical Review Letters 58(20): 2142 (1987).

58. Estler RC and Nogar NS, Applied Physics Letters 49(18): 1175-1177 (1986).

59. Danielzik B, Fabricius N, Röwekamp M and Von der Linde D, Applied Physics Letters 48(3): 212-214 (1986).

60. Burrell MC, Liu YS and Cole HS, Journal of Vacuum Science & Technology A 4(6): 2459-2462 (1986).

61. Masuhara H, Hiraoka H and Domen K, Macromolecules 20(2): 450-452 (1987).

62. Cole HS, Liu YS and Philipp HR, Applied Physics Letters 48(1): 76-77 (1986).

63. Feldmann D, Kutzner J, Laukemper J, MacRobert S and Welge KH, Applied Physics B 44(2): 81-85 (1987).

64. Brannon JH, Lankard JR, Baise AI, Burns F and Kaufman J, Journal of Applied Physics 58(5): 2036-2043 (1985).

65. Taylor RS, Singleton DL and Paraskevopoulos G, Applied Physics Letters 50(25): 1779-1781 (1987).

66. Taylor RS, Leopold KE, Singleton DL, Paraskevopoulos G and Irwin RS, Journal of Applied Physics 64(5): 2815-2818 (1988).

67. Simon P, Applied Physics B 48(3): 253-256 (1989).

68. Srinivasan R, Braren B and Dreyfus RW, Journal of Applied Physics 61(1): 372-6 (1987).

69. Dyer PE and Sidhu J, Journal of Applied Physics 57(4): 1420-1422 (1985).

70. Yeh JT, Journal of Vacuum Science & Technology A 4(3): 653-658 (1986).

71. Koren G, Applied Physics B 46(2):147-149 (1988).

72. Chuang MC and Tam AC, Journal of Applied Physics 65(7): 2591-2595 (1989).

73. Creasy WR and Brenna JT, Chemical Physics 126(2-3): 453-468 (1988).

74. Shin BS, Oh JY and Sohn H, Journal of Materials Processing Technology 187: 260-263 (2007).

75. Lazare S and Srinivasan R, The Journal of Physical Chemistry. 90(10): 2124-2131 (1986).

76. Braren B and Srinivasan R, Journal of Vacuum Science & Technology B 3(3): 913-917 (1985).

77. Torrisi L, Gammino S, Mezzasalma AM, Visco AM, Badziak J, Parys P, Wolowski J, Woryna E, Krása J, Láska L and Pfeifer M, Applied Surface Science 227(1-4): 164-174 (2004).

78. Womack M, Vendan M and Molian P, Applied Surface Science 221(1-4): 99-109 (2004).

79. Dyer PE, Oldershaw GA and Schudel D, Applied Physics B 51(5): 314-316 (1990).

80. Jensen MF, McCormack JE, Helbo B, Christensen LH, Christensen TR and Geschke O, Lab on a Chip 4(4): 391-395 (2004).

81. Romoli L, Fischer F and Kling R, Optics and Lasers in Engineering 50(3): 449-457 (2012).

82. Riveiro A, Soto R, Comesana R, Boutinguiza MD, Del Val J, Quintero F, Lusquiños F and Pou J, Applied Surface Science 258(23): 9437-9442 (2012).

83. Lasagni AF, Acevedo DF, Barbero CA and Mücklich F, Advanced Engineering Materials 9(1-2): 99-103 (2007).

84. Sumiyoshi T, Ninomiya Y, Ogasawara H, Obara M and Tanaka H, Applied Physics A 58(5):475-479 (1994).

85. Hiraoka H, Chuang TJ and Masuhara H, Journal of Vacuum Science & Technology B 6(1): 463-465 (1988).

86. Liu YS and Grubb WT, Method for photopatterning metallization via UV-laser ablation of the activator. US Patent US4882200A (1989).

87. Kim GD, Rundel JT and Paul BK, International Journal of Precision Engineering and Manufacturing 11(5): 665-671 (2010).

88. Skordoulis CD, Makropoulou M and Serafetinides AA, Applied Surface Science 86(1-4): 239-244 (1995).

89. Watanabe H and Yamamoto M, Journal of Applied Polymer Science 64(6): 1203-1209 (1997).

90. Yan Z, Huang X and Yang C, Microfluidics and Nanofluidics 21(6): 108 (2017).

91. Li M, Li S, Wu J, Wen W, Li W and Alici G, Microfluidics and Nanofluidics 12(5): 751-760 (2012).

92. Wolfe DB, Ashcom JB, Hwang JC, Schaffer CB, Mazur E and Whitesides GM, Advanced Materials 15(1): 62-65 (2003).

93. Hsieh YK, Chen SC, Huang WL, Hsu KP, Gorday K, Wang T and Wang J, Polymers 9(7): 242 (2017).

94. Huang H and Guo Z, Journal of Micromechanics and Microengineering 19(5): 055007 (2009).

95. Venkateswarlu G, Sharada R, and Rao MB, International Journal of Scientific and Research Publication 5(9): 560-568 (2015).

96. Becker W, Dahlin C, Becker BE, Lekholm U, Van Steenberghe D, Higuchi K and Kultje C, International Journal of Oral & Maxillofacial Implants 9(1): (1994).

97. Huber N, Heitz J and Bäuerle D, The European Physical Journal-Applied Physics, 25(1): 33-38 (2004).

98. Mitra A and Thareja RK, Journal of Materials Science 34(3): 615-619 (1999).

99. Wang ZB, Hong MH, Lu YF, Wu DJ, Lan B and Chong TC, Journal of Applied Physics 93(10): 6375-6380 (2003).

100. Yang Y, Wang S, Sun Z and Dlott DD, Applied Physics Letters 85(9): 1493-1495 (2004).

101. Liaw DJ, Wang KL, Huang YC, Lee KR, Lai JY and Ha CS, Progress in Polymer Science 37(7): 907-974 (2012).

102. Yu X, Ma J and Lei S, Journal of Manufacturing Processes 20: 349-355 (2015).

103. Sturesson C, Lasers in Surgery and Medicine 22(1): 51-57 (1998).

104. Dyer PE, Jenkins SD and Sidhu J, Applied Physics Letters 49(8): 453-455 (1986).

105. Niino H, Shimoyama M and Yabe A, Applied Physics Letters 57(22): 2368-2370 (1990).

106. Piruska A, Nikcevic I, Lee SH, Ahn C, Heineman WR, Limbach PA and Seliskar CJ, Lab on a Chip 5(12): 1348-1354 (2005).

107. Hautefeuille M, Cabriales L, Pimentel-Domínguez R, Velázquez V, Hernández-Cordero J, Oropeza-Ramos L, Rivera M, Carreón-Castro MP, Grether M and López-Moreno E, Lab on a Chip 13(24): 4848-4854 (2013).

108. Moon HY, Sidhu MS, Lee HS and Jeoung SC, Optics Express 23(15): 19854-19862 (2015).

109. Arenholz E, Kirchebner A, Klose S, Heitz J and Bäuerle D, MRS Online Proceedings Library Archive 526: 385-390 (1998).

110. Mansour N and Ghaleh KJ, Applied Physics A 74(1): 63-67 (2002).

111. Liu X, Du D and Mourou G, IEEE Journal of Quantum Electronics 33(10): 1706-1716 (1997).

112. Elaboudi I, Lazare S, Belin C, Talaga D and Labrugère C, Applied Physics A 92(4): 743-748 (2008).

113. Baudach S, Bonse J, Krüger J and Kautek W, Applied Surface Science 154: 555-560 (2000).

114. Klank H, Kutter JP and Geschke O, Lab on a Chip 2(4): 242-246 (2002).

115. De Marco C, Eaton SM, Suriano R, Turri S, Levi M, Ramponi R, Cerullo G and Osellame R, ACS Applied Materials & Interfaces 2(8): 2377-2384 (2010).

116. Zheng C, Hu A, Li R, Bridges D and Chen T, Optics Express 23(13): 17584-17598 (2015).

117. Efthimiopoulos T, Kiagias C, Heliotis G and Helidonis E, Canadian Journal of Physics 78(5-6): 509-519 (2000).

118. Blanchet GB, Macromolecules 28(13): 4603-4607 (1995).

119. Lippert T, Dickinson JT, Hauer M, Kopitkovas G, Langford SC, Masuhara H, Nuyken O, Robert J, Salmio H, Tada T and Tomita K, Applied Surface Science 197-198: 746-756 (2002).

120. Lippert T, Stebani J, Ihlemann J, Nuyken O and Wokaun A, The Journal of Physical Chemistry 97(47): 12296-12301 (1993).

121. Hauer M, Funk DJ, Lippert T and Wokaun AJ, Proceedings of SPIE 4760: 259-269 (2002).

122. Jeffers W, Seeley D, Faust RJ and Liu S, Preparation of diazo printing plates using laser exposure. US Patent US4248959 (1981).

123. Busman SC, Cuny GD, Zaklika KA and Ellis RJ, Diazo compounds for laser-induced mass transfer imaging materials US Patent US5756689A (1998).

124. Ma DL, Ma Y, Chen ZW and Hu AM, Journal of Materials Chemistry A 5(39): 20608-20614 (2017).

125. Yang CR, Hsieh YS, Hwang GY and Lee YD, Journal of Micromechanics and Microengineering 14(4): 480-483 (2004).

126. Riant I, Gurib S, Gourhant J, Sansonetti P, Bungarzeanu C and Kashyap R, IEEE Journal of Selected Topics in Quantum Electronics 5(5): 1312-1324 (1999).

127. Barnier F, Dyer PE, Monk P, Snelling HV and Rourke H, Journal of Physics D: Applied Physics 33(7): 757-759 (2000).

128. Snelling HV, Walton CD and Whitehead DJ, Applied Physics A 79(4-6): 937-940 (2004).

129. Jiang J, Callender CL, Noad JP, Walker RB, Mihailov SJ, Ding J and Day M, IEEE Photonics Technology Letters 16(2): 509-511 (2004).

130. Naessens K, Ottevaere H, Baets R, Van Daele P and Thienpont H, Applied Optics 42(31): 6349-6359 (2003).

131. Pan CT and Shen SC, Materials Science and Technology 20(2): 270-274 (2004).

132. Lan B, Hong MH, Kaidong DY, Chen SX and Chong TC, Proceedings of SPIE 4830: 196-201 (2003).

133. Cheng C, Wu J, Yu Y, Li R, Eda S, Chen J, Feng G, Lawrie B and Hu A, ACS Applied Materials & Interfaces 8(28): 17784-17792 (2016).

134. Trokel SL, Srinivasan R and Braren B, American Journal of Ophthalmology 96(6): 710-715 (1983).

CHAPTER 3. MACHINE VISION ASSISTED MICRO-FILAMENT DETECTION FOR REAL-TIME MONITORING OF ELECTROHYDRODYNAMIC INKJET PRINTING

Modified from a manuscript published in Procedia Manufacturing

Benjamin T. Lis[a], Yi Cai[b], Eric Spahr[a], Kevin Lin[a], Hantang Qin[a]

[a]*Industrial and Manufacturing Systems Engineering, Iowa State University, Ames, IA 50011;*

[b]*College of Science & Technology, North Carolina A&T State University, Greensboro, NC 27401*

Abstract

Electrohydrodynamic inkjet printing (e-jet printing) is one type of micro/nano scale 3D printing technique that automatically deposits functional materials to form 3D structures on the substrate. Unlike traditional thermal or acoustic inkjet printing, e-jet printing utilizes high electrical forces that enable the ink to overcome surface tension at the tip of micro nozzles. The droplets and filaments coming out from the nozzle have dimensions much smaller than the dimensions of the nozzle, thus printing geometries in micro and nano scale. E-jet printing process parameters could affect the final quality attributes of fabricated constructs. Currently, assessment of these critical geometries and attributes must be performed offline using optical microscopy or scanning electron microscopy. This drawback affected the efficiency of micro/nano printing from translation into industrial practice. The research in this paper focused on fundamental research to enable in-situ monitoring of e-jet printing using a real-time images characterization technique. In conclusion, the study in this paper investigated using machine vision for real-time monitoring of micro/nano scale 3D printing. The method worked well for micro-filament detection in e-jet printing, and may be

further implemented into feedback control system of complicated e-jet printing. However, the optical machine vision was limited to micro scale detection. One of the future research topic is to develop nano scale in-situ detection mechanism for e-jet printing. This monitoring method has potential in a hybrid manufacturing system involving laser ablation and E-jet printing.

Introduction

Additive manufacturing has been playing a significant role in academia and industry over the last two decades [1]. The commonly recognized term 3D printing was one straightforward way to describe how additive manufacturing works [2]: complex objects based on various functional materials were achieved with the help of an elegant layer-by-layer concept [3-5]. Inkjet based 3D printing was one of the additive manufacturing techniques that showed its great advantages including high customization, design flexibility, low-cost, easy setup, and controllability [6-8]. However, challenges have popped up in inkjet 3D printing when high-resolution features were required. It was difficult for thermal or acoustic based inkjet printing to print patterns within 20 μm [9-11], because higher resolutions of printed patterns required smaller nozzles. As nozzle dimensions approached sub-20 μm, surface tension of materials would prevent filament and droplet formation at the tip of the nozzle. In addition, the cost to manufacture nozzles would also be increased.

Electrohydrodynamic inkjet printing (e-jet printing) was proposed to resolve resolution issues in micro/nano field associated with traditional thermal or acoustic inkjet printing [12]. By applying and controlling a high voltage between the nozzle and bottom substrate, the ink at tip of nozzle worked in Tyler-cone mode. This generate a stable and fine jet (for polymers) or droplets (for metal particles), whose dimensions were much smaller than

the size of the nozzle. Gold nanoparticles [13], silver colloids [14], copper ink [15], and biopolymers [16] have all been reported in the past few years using e-jet printing. As a relatively new technique closely related to material science, there were still plenty of challenges. First, each new ink material needed to be characterized for e-jet printing systems. Conductivity, viscosity, particle sizes, and solvent property all affect printing conditions. Second, performance of printed product also needed to be characterized, including mechanical properties, electrical performance, biomechanics, etc. Third, mathematical models and simulations for e-jet printing related to specific materials needed to be further investigated [17, 18].

In order to solve the challenges of e-jet printing for micro/nano scale fabrication, a vision system was necessary. This vision system could capture formation of droplets/filaments and their flight behavior during printing, which was key to investigate mechanisms of ink dynamics. Different optical lenses and cameras were used in all e-jet printing systems for this purpose [19, 20]. Byun et al. used a high-speed-camera to capture flight behavior of charged droplets in e-jet printing, which led to a better understanding of electrical fields during printing [21]. Chung et al. investigated pulsating droplet mode for various voltage settings with the help of a charged couple device (CCD) camera and zoom lens. The time resolved images for different voltage configurations were demonstrated for meniscus fluid dynamic analysis [22]. Post processing on the images and videos after printing was also researched by several groups for development of feedback loop control in e-jet printing systems. Wang et al. proposed stroboscopic imaging technique for voltage adjustment to characterize printing conditions [23]. All of the attempts to use optical images

for monitoring e-jet printing systems actually were the first step for machine vision automation systems.

Machine vision was a broader term that included all technologies and methods that extract information from images to provide image-based automatic inspection and analysis for system automation [24]. A general machine vision system consisted of major components including illumination, cameras, image digitization algorithms, and image analysis [25]. The technique has been used increasingly in additive manufacturing [26-28] for inspection and evaluation purposes as it provides rapid, economic, consistent, and objective feedback and assessment. Faes et al. reported laser scanning for extrusion based 3D printing by capturing geometrical 3D data from scanning images [29]. Hu et al. delivered real-time sensing and control for additive manufacturing based on infrared image sensing, which was also verified with finite element model [30]. Kwon worked on CCD images for inkjet printing system and measured speed information based on edge detection [31]. Those previous works tried to set up a robust system for better product quality in different additive manufacturing techniques. However, the machine vision system for versatile e-jet printing in micro/nano scale was still under investigation. Traditionally, real-time quality inspection for e-jet printing has been performed by human operators. However, the manual inspections were time-consuming and labor-intensive. Moreover, the accuracy of tests cannot be guaranteed.

The first objective was to investigate limitations of optical machine vision systems for the next-stage of software and system updates. The second objective of research was to determine all scenarios in e-jet printing using machine vision. Algorithms were developed to process images corresponding to all representative scenarios. In this paper, the focus was to develop real-time inspection mechanism for e-jet printing. Machine vision concept was

adapted into e-jet printing system for micro/nano filaments and droplet detection. The basic principle of machine vision systems was investigated. The core of machine vision system for e-jet printing was image processing and image analysis. The algorithm and methods were presented in the paper. The results demonstrated convincing results for machine vision to be used as real-time monitoring technique for micro-filament detection. This paper introduced the machine vision setup and methodology used and then discussed experimental results obtained.

Machine Vision

The lab-built e-jet printing system was able to print out micro-scale polymer filament and achieve high-resolution patterns. However, one of the challenges in the fields was inspection and quality control because manual inspection was time-consuming and labor-intensive. As of now, the in-situ quality control of e-jet printing in the micro/nano scale has not been fully explored. Advances in this area have the potential to significantly reduce and prevent defects, saving time and money. In this paper, a machine vision system for real-time monitoring of e-jet printing was demonstrated. A static image of e-jet printing was shown in Fig. 1 (c). The detailed theory of e-jet printing was not the focus of this paper, hereby it was not covered here. Previous publications [32-34] of the authors have clearly explained process control and material characterization of e-jet printing. The images showed symmetry because the printing substrate was glass, which reflected the shape of nozzle and micro filaments. The diameter of nozzle was measured using microscopes, which was used as reference dimensions for image processing, as shown in Fig. 1 (b).

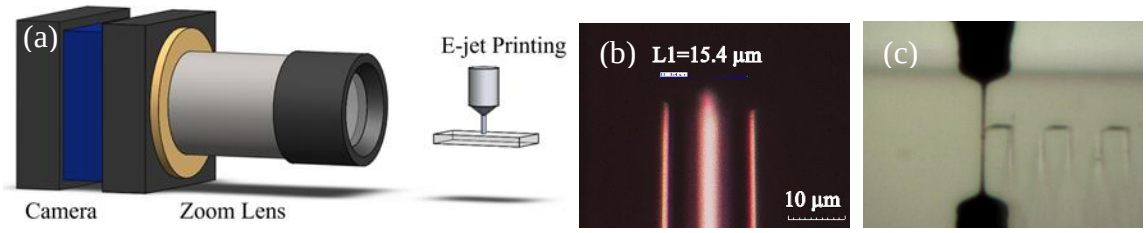

Fig. 1. (a) Illustrative drawing of system setup; (b) nozzle measurement using microscope; and (c) e-jet printing of micro-scale polymer filament.

Illustrative drawing of the system set up was demonstrated in Fig. 1 (a). For the zoom lens, working distance was 86mm, depth of fields was between 0.05mm and 1.39mm at highest and lowest magnification, horizontal FOV was between 0.35mm and 4.18mm at highest and lowest magnification. For the camera, pixel size was 4.8 μm x 4.8 μm, horizontal sensor size 6.14mm, and vertical sensor size 4.92 mm.

The basic principle and philosophy of the machine vision system developed was described in Fig. 2. The ultimate goal was to finish closed-loop system control for e-jet printing. The machine vision system developed in this paper would be the first step. As shown in Fig. 2, the image was captured by a zoom lens and a camera at a controllable rate up to 168 frames per second. The two-dimensional images were then enhanced and processed into black and white binary data. With a fixed threshold and dimensions of nozzle known, images were processed based on pixel information. The future steps include the quality inspection system, which produces the actual deposition rate as a result of observations and calculations by the vision system. This would then be compared to the theoretical input rate and any discrepancies are then identified. The last step is the adjustment of the process parameters to eliminate these discrepancies.

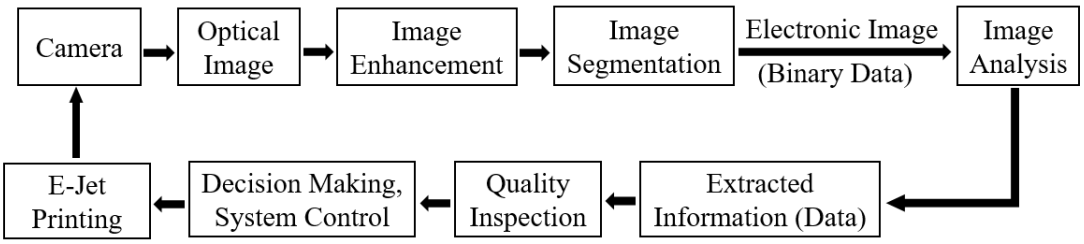

Fig. 2. Principle and philosophy of machine vision system

Methodology

Resolution Analysis of Zoom Lens and Camera

To eliminate time-consuming labor inspection, reliability of the monitoring system was first investigated. Before setting up the machine vision system for e-jet printing, the first question was always how reliable the data would be.

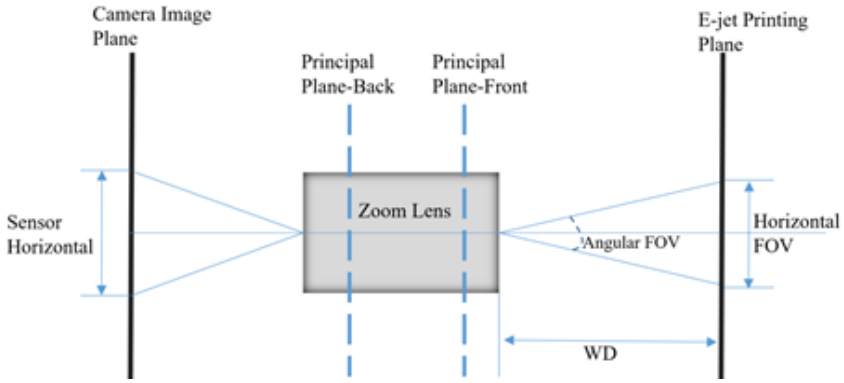

Fig. 3. Setup of zoom lens and camera: relationship for magnification and space resolution limit

It was hard to maintain the working distance precisely at 86mm all the time. The basic light projection for the zoom lens and camera was described in Fig. 3. Assuming the angular FOV changed as a function of WD, the prescribed WD along with horizontal FOV were given as specifications, the AFOV could be calculated based on Equation (1).

$$AFOV(^\circ) = 2 * \tan^{-1}\left(\frac{HorizontalFOV(mm)}{2 * WD(mm)}\right) \quad (1)$$

The AFOV was 2.784 degrees at the lowest magnification and 0.2332 degrees at the highest magnification. The magnifications could be altered to different level by adjusting lens and adapter. However, AFOV would remain the same at maximum and minimum magnifications. The AFOV would be used to calculate how HFOV would be changed at various working distances. This would in turn affect the PMAG and object space resolution which were calculated by Equations (2) and (3).

$$PMAG = \frac{Sensor\ Size(mm)}{FOV(mm)} \tag{2}$$

$$OSR = \frac{Pixel\ Size(\mu m)}{PMAG\ of\ System} \tag{3}$$

The ideal WD of 86mm resulted in an object space resolution at low magnification (OSRL) of 3.26 μm and an object space resolution at high magnification (OSRH) of 0.2735 μm. The linear relationship was shown in Fig. 4. The zoom lens and camera were always working at maximum magnification level. As a result, the change in working distance only slightly affected the object space resolution, and the OSRH was always smaller than 0.5 μm.

Every lens has a finite aperture, and diffraction occurs when light passes through apertures. Airy disk phenomena was a result of diffraction patterns where a series of concentric rings with decreased intensity covered center of a bright spot. As multiple Airy patterns from different details on target filaments came close together, they would overlap and generate constructive interference to reduce the resolution and contrasts. If the lens and camera setup couldn’t distinguish the microfilaments clearly, the images could not be referred for inspection.

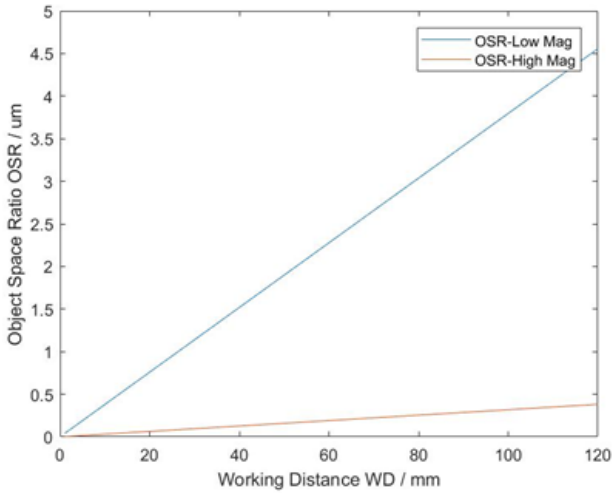

Fig. 4. Relationship between working distance and object space ratio at low and high magnification level

The NA for the zoom lens was a specification listed as 0.019 at lowest magnification and 0.101 at highest magnification. Each lens has an absolute upper performance limit dictated by laws of physics. The limitation as mentioned was controlled by working f/# and wavelength of lights that pass through. The diffraction limit of the system setup thus could be calculated using Equation (4) and (5), known as line pairs/mm, which determines theoretical maximum resolving power of the system. The diffraction limit could be converted into object space resolution OSR in μm using Equation (6).

$$NA = \frac{1}{2 * \left(\frac{f}{\#}\right)} \tag{4}$$

$$Diffraction\ Limit\left(\frac{lp}{mm}\right) = \frac{1000\mu m/mm}{\frac{f}{\#} * Wavelength(\mu m)} \tag{5}$$

$$OSR = \frac{\frac{1000\mu m}{mm}}{2 * OSR\left(\frac{lp}{mm}\right)} \tag{6}$$

The results were 8.327 μm for lowest magnification and 1.566 μm for highest magnification of the zoom lens. This indicated that, at micro-scale detection, the limiting factor was the diffraction limit as these resolution values were significantly higher than the ones produced by a varying WD. The resolution was significantly affected by numerical aperture (NA) and wavelength of light used in the system. In the following experiments, all dimensions in the machine vision system were greater than 5 μm to make sure that the data acquired from the lens and camera was reliable.

Imaging Processing Algorithm

In order to obtain the information of interest from an image such as the diameter of the filament being deposited, an image processing algorithm was developed which included a series of steps. These steps were explained as below.

Grayscale Transform and Thresholding

Depending on the camera being used and its image acquisition configuration, the obtained images could be either color or gray-scale. If an obtained image was already in grayscale, it was ready for further transformation into a binary image. If an obtained image was a color one, it needed to be transformed into grayscale based on the Red Green Blue (RGB) values in each pixel using the following Equation (7) [35]. This is a generally accepted grayscale conversion formula used in a variety of encoding systems.

$$Grayscale = 0.3 * R + 0.6 * G + 0.1 * B \quad (7)$$

After an image was transformed into grayscale, it needed to be further transformed into a binary image before image processing techniques like blob analysis and morphological operations could be properly implemented. As its name indicated, a binary image had only two colors, and black and white were used most often. During the binary transformation,

each pixel in a grayscale image was set to be one of these two colors, depending on whether its grayscale value was greater or lower than a predefined threshold value. Given the strong contrast between the foreground (nozzles, ink, etc.) and the background, which would be demonstrated by the figures shown in the next section, Otsu's method for thresholding [25] was used to obtain a suitable required threshold value for the binary transformation. In our case, pixels with a grayscale value greater than the threshold value were set to white RGB (255, 255, 255), while those with a grayscale value lower than the threshold value were set to black with RGB (0, 0, 0).

Blob Analysis for Nozzle

To obtain length and diameter information of the filament, it was important to determine the measurement scale between the actual distance and image pixels. In other words, the actual distance each pixel in the image represents needed to be investigated, or μm/pixel. In this case, the nozzle used in E-jet printing would be a good reference, because its diameter was known. To automate the real-time monitoring processing, it was desirable that the software could automatically identify the nozzle in an image, and then used it as reference for remaining calculations regarding length, diameter or distance.

Blob Analysis was a fundamental technique of machine vision based on analysis of consistent image regions. A blob was a region of an image in which some properties were constant or approximately constant [36]. In our case, a blob was a cluster of connected pixels which had the same color in the binary image. Such a blob usually represented an actual entity such as the nozzle.

To use the nozzle as reference, an image could be taken before the deposition began. Blob analysis could be then applied to this image after binarization. One or more blobs would be identified. Due to its large size and location (on top) in the image, the blob corresponding

to the nozzle could be easily identified, and its diameter in pixels could be measured. By associating this diameter in pixels with the nozzle's actual diameter, the measurement scale could be determined. It would be used for the subsequent calculation.

Determination of Region of Interest (ROI)

After the nozzle was identified in an image and the measurement scale was calculated, it was possible and desirable to determine a region of interest (ROI) for remaining steps. Such a ROI could save the computation time in the remaining processing steps compared to using the whole image. It also mitigated the interferences of other elements in the image, such as printed patterns, substrate edges, etc.

Simply, the ROI could be defined as a rectangular area below the nozzle in the image. The width was set to be the diameter of the nozzle, or even smaller, while the height of the rectangle was set to be 90% of the deposition height of the nozzle, which could be obtained from the control data. This was because the filament being deposited, which we were most interested in, normally lies in this region.

Morphological Operations

The threshold value determined to generate the binary image could not eliminate all noises. For example, small particles of dust tended to attach to the camera lens, which was often observed in our experiments. Therefore, two morphological operations, namely erosion and dilation [37], were used.

The purpose of erosion was to shrink borders of foreground objects which include the nozzle, filament and noises, if any. Hence, the foreground objects became smaller and the holes in the objects became larger. In our case, it helped to remove the noises, which usually took up only several pixels. The dilation operation aimed to expand the borders of the foreground objects. Thus, the foreground objects became larger and the holes in the objects

became smaller or disappear completely. In our case, it helped to compensate for the erosion operation so that the measurement was more accurate. Since small objects were eliminated by erosion, they could not appear in dilation operation again. Details of erosion and dilation operation could be found in [37]. In addition to the morphological operations, blob analysis could also be implemented in the ROI again to rule out the noises based on blob sizes.

Processing of ROI

At this point, the ROI should be a clean binary image containing only the contour of the filament. Although printed patterns on the substrate or substrate edges sometimes appeared within this region in the original grayscale image, it was found that they could be effectively removed during the binary transformation, as would be demonstrated later in Figs. 7-10. This was because the printed patterns were not in the focal plane of the lens, and they were significantly blurred due to the short depth of view in a microscopic lens. Their grayscale values were closer to the background, so they were wiped out in the binary image.

The calculation of filament diameter was straightforward by counting the pixels in the horizontal direction and multiplying the pixel number with the measurement scale. Depending on the requirements, the diameter at specific distance from the nozzle or the average diameter of the filament in air could be calculated. Straight lines or parabolic curves could be applied to model the shape and tilting of the filament. Discussion of the results was presented in Section 4.

3D Rendering

3D reconstruction algorithms were developed to mimic printed patterns based on detected material flow. A series of planes cut the binary images were selected, as shown in Fig. 5. Assuming the cross-section profile of the nozzle and micro-filaments were circular, the circle in each layer using polygons lines could be approximated, as shown in Fig. 5 (c)

and (d). The diameter of the circles were determined by pixel numbers based on previous algorithms. The layer 1 and 2 were used as example here for 3D reconstruction.

Depending on how many segments (n in Fig.5 (c) and (d)) used to approximate the circle, the coordinates of the polygon vertices (A1, A2, B1, and B2) were determined using single trigonometry sine and cosine functions. For layer 1, if n=12, the coordinate of A1 was defined as (x, y, z) = (RAcos240°, RAcos240°, HA), where RA was the radius of the circle in layer 1, HA was the relative height of layer 1 shown in Fig.5 (a) with respect to z=0 position. The coordinate values of A2, B1, and B2 could be calculated using the same method.

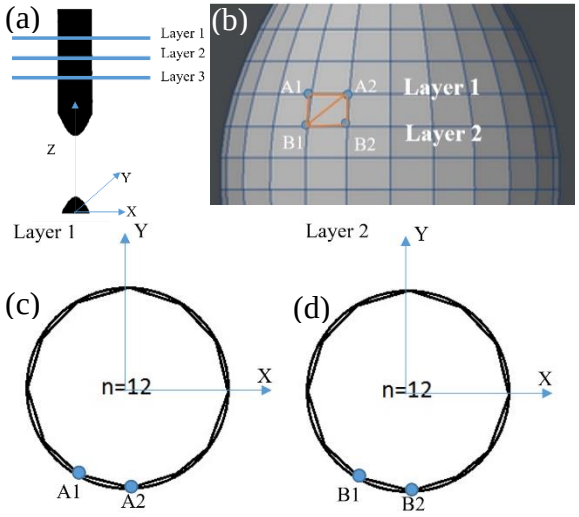

Fig. 5. (a) Coordinate system of constructed 3D model of nozzle and micro-filament; (b) constructed 3D object based on pixel dimensions; (c) polygons segments of layer 1; and (d) polygon segments of layer 2

The illustrate graph of how to achieve 3D features was demonstrated in Fig. 5. (b). Once coordinate values of A1, A2, B1, and B2 were obtained, OpenGL function GL_TRIANGLES was applied twice to generate two triangle facets determined by the four points. The first triangle consisted of A1, A2, and B1, and the second B1, B2, and A1. After iterating this algorithms for all the vertices of the polygon in all layers, the 3D surface object

could be generated for display. When repeating the procedures to create the meshed 3D structure, HA of A1 and A2 shared same value, and HB of B1 and B2 shared same value.

Computer Interface Design and Results Analysis

Computer interface design was shown in Fig. 6. The camera took images at frame rate up to 160 frames per second. The image directory was loaded to the software package automatically so that the real-time monitoring was achieved. The camera takes images successively at a frame rate of 100fps. The software package reads all images through their location directory. Each image would be cropped or processed through algorithms only focusing on regions of interests (ROI). Each colored image was converted to both grayscale and binary images. Pixel numbers and histogram information along any horizontal and vertical lines could be set up and measured. Input windows also allow manual threshold input and nozzle dimensions input.

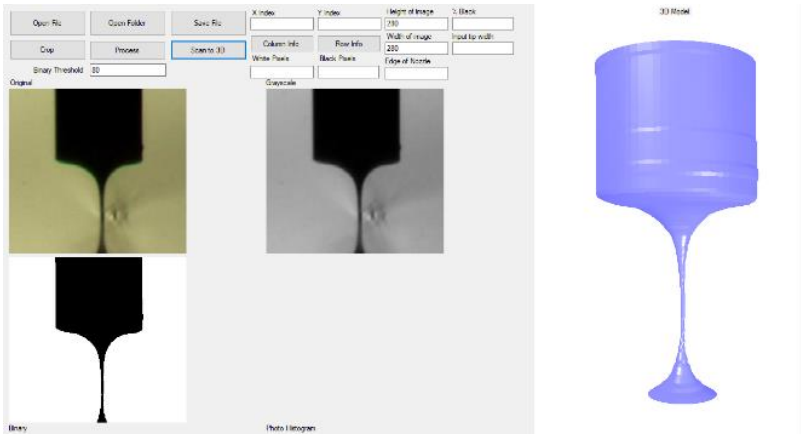

Fig. 6. Computer interface design

Results and Discussion

Normal Printing for Binary Threshold Testing

It was impossible to develop a binary conversion algorithm without pre-tested database as threshold optimal solutions. The philosophy was that the conversion algorithm

would identify each scenarios and pick up the optimized binary threshold to determine what should be converted to black and what should be converted to white. Ideally, only the nozzle area was black and everything else in the images was white. If colored images were used, more accurate algorithms may be developed depending on pixel information for different colors.

As shown in Fig.1 (c), the images captured from the camera showed the tip of the nozzle in Taylor-cone mode and the ink coming from the nozzle, on both sides of a mirror surface (glass slides in the experiments). Depending on what angle the picture was taken from, this may be a simple or complex problem. Algorithms to eliminate the mirrored surface on each image would be developed. It was possible to simply take half of the total length of reflected ink and regular ink since majority of images showed the reflected part of the image halfway down. For other scenarios which were discussed in the following sections, that simple algorithm was not applicable. The point where the reflected image begins was difficult to ascertain. One representative processed image of scenario 1 was shown in Fig 7.

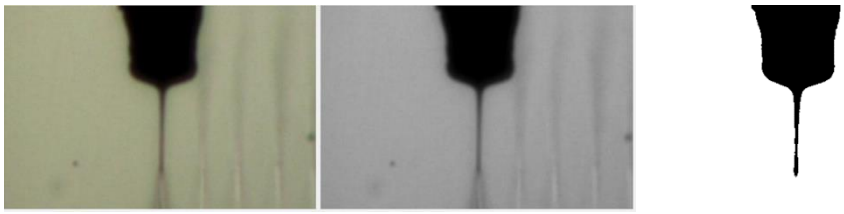

Fig. 7. Normal printing for binary threshold testing

Detection for Changes of Dimensions

As the nozzle moved throughout the printing, the dimensions of microfilaments coming out were subject to changes due to variations in printing conditions. The software package was the first step in the feedback loop control system. Since the movement of stages was pre-programmed, it was possible to reconstruct the 3D model of printed pattern based on

dimensions collected in real time. If the dimensions went off, the printing could be paused and variable inputs could be adjusted to account for any errors or defects. The illuminating system was precisely controlled to make sure the interference of lighting on binary conversion was minimized.

Fig 8. demonstrated changes of dimensions during printing with increased voltages as inputs. The red rectangle marked area of interests where dimensions were calculated and averaged. The red circled area showed possible interference in image processing when printed pattern were present.

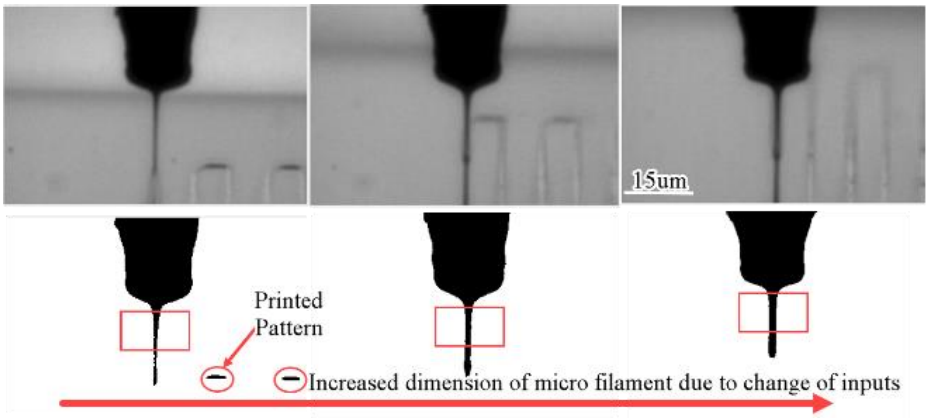

Fig. 8. monitoring changes of dimensions during printing

Tilted Micro-Filaments When Printing in Different Orientations

Some images appeared to feature a diagonal stream of ink. This was due to the movement of the substrate as the ink came out. As the ink made a contact with substrate, the micro-filament in the air would be lagged and dragged as movement continued. In fact, all images would feature a slight “bending” effect. The primary concern here was to remove this “bending” effect from pictures of the horizontal movement. The tilted angle information was critical because it may also affect simulation of e-jet printing at different working speeds.

A step towards resolving this would be to determine the angle information of the filament. A tangent line could be drawn halfway down the filament and its angle (a) to the normal measured, as shown in Fig. 9. This piece of information would be useful when converting the 3D model of the nozzle to a 3D model of the printed pattern.

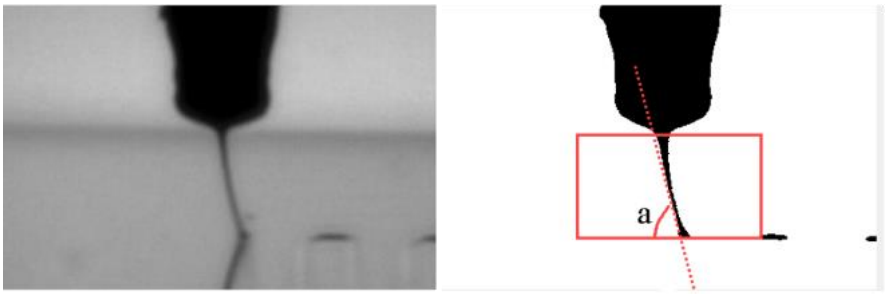

Fig. 9. emphasis on diagonal stream

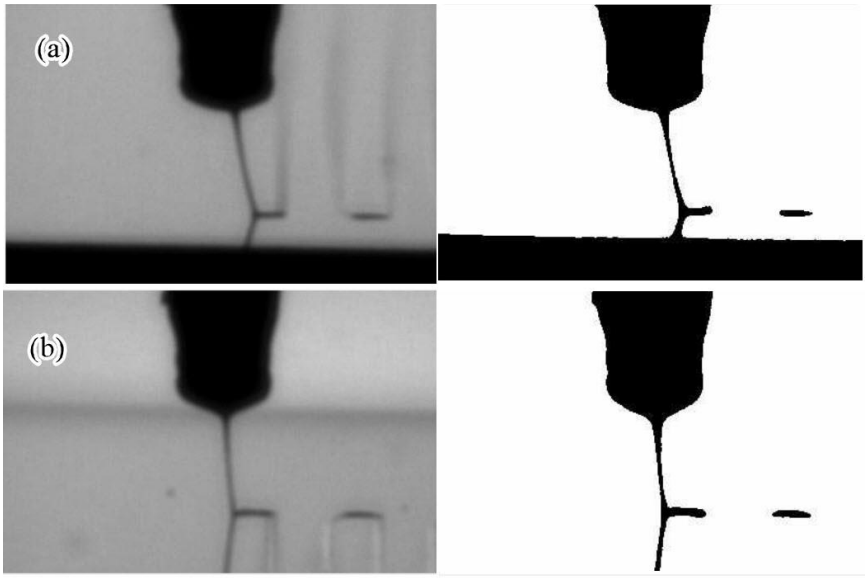

Fig. 10. printing on the edge of substrate

Printing on the Edge of Substrate

As the printing neared the edge of the substrate, it may be difficult to obtain a clear binary picture, since the edge of the substrate would block lights and be very dark. If the

printing was on the bottom of the substrate, the same algorithm that removes the mirrored effect should be able to remove that edge with little modification, as shown in Fig 10. (a).

While printing near the top of the substrate, it may be necessary to take one more step to focus on only the interested area of the image. It would be fairly easy to differentiate the edge of the substrate from the filament and nozzle because the edge would span the entire image, while the nozzle and filament would be considerably narrower.

A bigger issue with this scenario was that the horizontal ends of the pattern register as black; this makes it hard to differentiate between ink coming from the nozzle and the ink that has already been printed along that horizontal line.

Multi-Layer Printing, Interference of Printed Pattern

This was the most difficult of these five scenarios. Monitoring the printing process for the first pass would be relatively simple. However, e-jet printing required multiple passes to build up material on the substrate. The task here was to differentiate details of the current layer from patterns that have already been printed underneath the current layer. Determining which features were part of the current layer verses previous layers would be a complex task. Although not complete, a good step in the right direction was to determine the precise distance between the nozzle and the substrate. This helped to indicate where the printing was currently happening.

The binary conversion for this scenario was also a challenge. Past layers showed up at the same threshold as the filament. Thus, it was beneficial to develop a method to indicate whether ink was coming from the nozzle or if it has already been printed. Developing an algorithm to establish which ink was below (coming from) the nozzle and which ink was adjacent (already been printed) was our next step towards solving this problem.

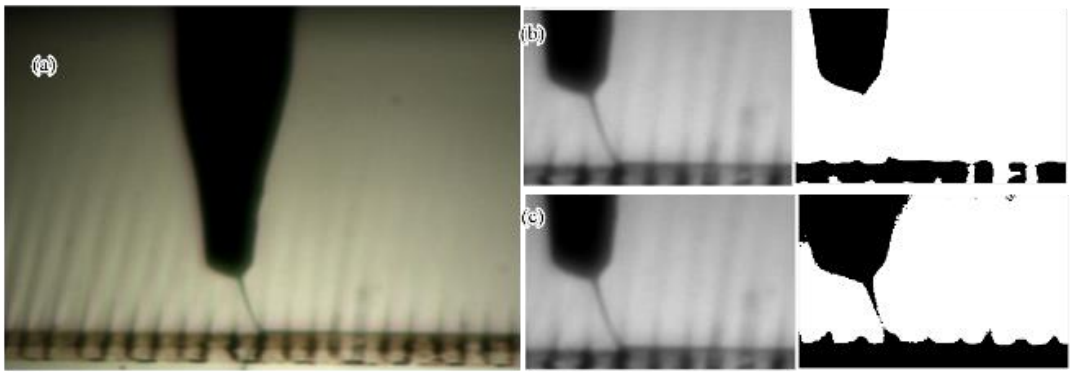

Fig. 11. Multi-layer printing challenges

There was clearly an issue with the binary conversion process that must be resolved before proper modelling could be done. The other images in this set all yield similar results. A method for properly binarizing the original image must be developed for this scenario to be resolved. Additionally, a method for tracking material flow will need to be established. After a layer completes, a snapshot of the printed formation can be stored by the vision system. As the next layer prints, images that are unclear can be checked against that snapshot to evaluate which material is new and which material belongs to previous layers. This method is currently being developed.

Focused Area of Sample Filament Imaging

There were different strategies to optimize image processing, shorten processing time, and reduce memory consumption. One that was used in real-time monitoring was to only process images in focused regions of interests. There were pre-defined openCV function that may be applied into the current package, such as blob analysis and Otsu's methods for adaptive binarization. The paper was based on the first and original version of the software package developed in the lab. Plenty of updates have been applied to the first version, and would be reported in the conference reports.

Fig. 12. Micro-filament detection in focused regions of interests

Challenges and Future Research Topics

As mentioned in Section 2, the ultimate goal of this research was to finish closed-loop controlling system for e-jet printing, to achieve real-time monitoring and quality control. With dimensions analyzed from the 2D image, any changes in polymer flow would be captured. For e-jet printing, the nozzle was fixed and bottom substrate was moving to achieve pattern features. In this case, as long as stage movement was pre-programmed, the dimensional information from 3D image and movement of stage combined could be used to simulate three-dimensional structure achieved. This would be a wonderful tool to realize quality control of printed pattern and to figure out correction mechanism and algorithms if any defects happens during printing.

Another future topic that the group was working on was related to algorithm and system optimization. The camera was able to capture 168 images within one seconds, roughly 10,000 images within one minute. That was huge amount of data to process if real-time monitoring was to be implemented. The group continuously worked on algorithm optimization during all-stage system optimization.

Conclusion

One of the biggest challenges and drawbacks in current 3D printing systems was a lack of real-time monitoring and quality control system. The difficulty for such a system

increased exponentially when it came to detection for micro/nano 3D printing. The translation of micro/nano 3D printing into industrial practice was thus affected. The study in this paper investigated micro and nano scale real-time monitoring methods for e-jet printing, which could be generalized into other micro printing systems.

The study first investigated limitations of optical machine vision systems, including a zoom lens and CMOS camera. Different scenarios in e-jet printing using machine vision were then discussed. The real-time inspection mechanism for e-jet printing was developed and machine vision concept was adapted into e-jet printing system for micro/nano filaments and droplets detection.

In conclusion, at the micron level, changing the working distance of the zoom lens didn't affect resolution much. Resolution was significantly affected by NA and wavelength of the light used. The data from the zoom lens and camera system was reliable for calculating dimensional information. The results demonstrated convincing results for machine vision to be used as real-time monitoring technique for micro-filament detection. The method worked well for micro-filament detection in e-jet printing, and may be further implemented into feedback control system of complicated e-jet printing. However, the optical machine vision was limited to micro scale detection. One of the future research topic is to develop nano scale in-situ detection mechanism for e-jet printing. The lab-developed software package was subject to many updates. All the updating information would be reported in the conference presentations.

References

[1] I. Gibson, D. W. Rosen,B. Stucker, Additive manufacturing technologies. Vol. 238. Springer. 2010.

[2] B. P. Conner, G. P. Manogharan, A. N. Martof, L. M. Rodomsky, C. M. Rodomsky, D. C. Jordan,J. W. Limperos, Making sense of 3-D printing: Creating a map of additive manufacturing products and services. Additive Manufacturing, 1, (2014) 64-76.

[3] W. E. Frazier, Metal additive manufacturing: a review. Journal of Materials Engineering and Performance, 23(6), (2014) 1917-1928.

[4] F. P. Melchels, M. A. Domingos, T. J. Klein, J. Malda, P. J. Bartolo,D. W. Hutmacher, Additive manufacturing of tissues and organs. Progress in Polymer Science, 37(8), (2012) 1079-1104.

[5] K. V. Wong,A. Hernandez, A review of additive manufacturing. ISRN Mechanical Engineering, 2012, (2012).

[6] M. Singh, H. M. Haverinen, P. Dhagat,G. E. Jabbour, Inkjet printing—process and its applications. Advanced materials, 22(6), (2010) 673-685.

[7] B. Derby, Inkjet printing of functional and structural materials: fluid property requirements, feature stability, and resolution. Annual Review of Materials Research, 40, (2010) 395-414.

[8] G. Cummins,M. P. Desmulliez, Inkjet printing of conductive materials: a review. Circuit World, 38(4), (2012) 193-213.

[9] B. Derby, Bioprinting: inkjet printing proteins and hybrid cell-containing materials and structures. Journal of Materials Chemistry, 18(47), (2008) 5717-5721.

[10] G. Gao,X. Cui, Three-dimensional bioprinting in tissue engineering and regenerative medicine. Biotechnology letters, 38(2), (2016) 203-211.

[11] X. Cui, T. Boland, D. D D'Lima,M. K Lotz, Thermal inkjet printing in tissue engineering and regenerative medicine. Recent patents on drug delivery & formulation, 6(2), (2012) 149-155.

[12] J.-U. Park, M. Hardy, S. J. Kang, K. Barton, K. Adair, D. kishore Mukhopadhyay, C. Y. Lee, M. S. Strano, A. G. Alleyne,J. G. Georgiadis, High-resolution electrohydrodynamic jet printing. Nature materials, 6(10), (2007) 782.

[13] S. Samarasinghe, I. Pastoriza-Santos, M. Edirisinghe, M. Reece,L. M. Liz-Marzán, Printing gold nanoparticles with an electrohydrodynamic direct-write device. Gold Bulletin, 39(2), (2006) 48-53.

[14] D.-Y. Lee, Y.-S. Shin, S.-E. Park, T.-U. Yu,J. Hwang, Electrohydrodynamic printing of silver nanoparticles by using a focused nanocolloid jet. Applied Physics Letters, 90(8), (2007) 081905.

[15] A. Khan, K. Rahman, D. S. Kim,K. H. Choi, Direct printing of copper conductive micro-tracks by multi-nozzle electrohydrodynamic inkjet printing process. Journal of materials processing technology, 212(3), (2012) 700-706.

[16] A. Gupta, A. M. Seifalian, Z. Ahmad, M. J. Edirisinghe,M. C. Winslet, Novel electrohydrodynamic printing of nanocomposite biopolymer scaffolds. Journal of bioactive and compatible polymers, 22(3), (2007) 265-280.

[17] W. Wei, Z. Gu, S. Wang, Y. Zhang, K. Lei,K. Kase, Numerical simulation of the cone–jet formation and current generation in electrostatic spray—modeling as regards space charged droplet effect. Journal of Micromechanics and Microengineering, 23(1), (2012) 015004.

[18] M. S. Onses, E. Sutanto, P. M. Ferreira, A. G. Alleyne,J. A. Rogers, Mechanisms, capabilities, and applications of high-resolution electrohydrodynamic jet printing. Small, 11(34), (2015) 4237-4266.

[19] M. Lee, D. Kang, N. Kim, H. Kim, S. James,S. Yoon, A study of ejection modes for pulsed-DC electrohydrodynamic inkjet printing. Journal of Aerosol Science, 46, (2012) 1-6.

[20] B. W. An, K. Kim, H. Lee, S. Y. Kim, Y. Shim, D. Y. Lee, J. Y. Song,J. U. Park, High-Resolution Printing of 3D Structures Using an Electrohydrodynamic Inkjet with Multiple Functional Inks. Advanced materials, 27(29), (2015) 4322-4328.

[21] H. T. Yudistira, V. D. Nguyen, P. Dutta,D. Byun, Flight behavior of charged droplets in electrohydrodynamic inkjet printing. Applied Physics Letters, 96(2), (2010) 023503.

[22] S. Lee, J. Song, H. Kim,J. Chung, Time resolved imaging of electrohydrodynamic jetting on demand induced by square pulse voltage. Journal of Aerosol Science, 52, (2012) 89-97.

[23] T. Wang, T.-H. Kwok,C. Zhou, In-situ Droplet Inspection and Control System for Liquid Metal Jet 3D Printing Process. Procedia Manufacturing, 10, (2017) 968-981.

[24] R. Jain, R. Kasturi,B. G. Schunck, Machine vision. Vol. 5. McGraw-Hill New York. 1995.

[25] E. R. Davies, Machine vision: theory, algorithms, practicalities: Elsevier. 2004.

[26] M. Grasso, V. Laguzza, Q. Semeraro,B. M. Colosimo, In-process monitoring of selective laser melting: Spatial detection of defects via image data analysis. Journal of Manufacturing Science and Engineering, 139(5), (2017) 051001.

[27] M. Khanzadeh, S. Chowdhury, L. Bian,M. A. Tschopp. A Methodology for Predicting Porosity From Thermal Imaging of Melt Pools in Additive Manufacturing Thin Wall Sections. in ASME 2017 12th International Manufacturing Science and Engineering Conference collocated with the JSME/ASME 2017 6th International Conference on Materials and Processing. (2017). American Society of Mechanical Engineers, Volumn, (Year) V002T01A044-V002T01A044.

[28] M. Grasso, A. Demir, B. Previtali,B. Colosimo, In situ monitoring of selective laser melting of zinc powder via infrared imaging of the process plume. Robotics and Computer-Integrated Manufacturing, 49, (2018) 229-239.

[29] M. Faes, W. Abbeloos, F. Vogeler, H. Valkenaers, K. Coppens, T. Goedemé,E. Ferraris, Process monitoring of extrusion based 3D printing via laser scanning. arXiv preprint arXiv:1612.02219, (2016).

[30] D. Hu,R. Kovacevic, Sensing, modeling and control for laser-based additive manufacturing. International Journal of Machine Tools and Manufacture, 43(1), (2003) 51-60.

[31] K.-S. Kwon, Speed measurement of ink droplet by using edge detection techniques. Measurement, 42(1), (2009) 44-50.

[32] C. Wei, H. Qin, N. A. Ramírez-Iglesias, C.-P. Chiu, Y.-s. Lee,J. Dong, High-resolution ac-pulse modulated electrohydrodynamic jet printing on highly insulating substrates. Journal of Micromechanics and Microengineering, 24(4), (2014) 045010.

[33] C. Wei, H. Qin, C.-P. Chiu, Y.-S. Lee,J. Dong, Drop-on-demand E-jet printing of continuous interconnects with AC-pulse modulation on highly insulating substrates. Journal of Manufacturing Systems, 37(2), (2015) 505-510.

[34] H. Qin, J. Dong,Y.-S. Lee, AC-pulse modulated electrohydrodynamic jet printing and electroless copper deposition for conductive microscale patterning on flexible insulating substrates. Robotics and Computer-Integrated Manufacturing, 43, (2017) 179-187.

[35] C. Saravanan. Color image to grayscale image conversion. in Computer Engineering and Applications (ICCEA), 2010 Second International Conference on. (2010). IEEE, Volumn, (Year) 196-199.

[36] S. Hinz. Fast and subpixel precise blob detection and attribution. in Image Processing, 2005. ICIP 2005. IEEE International Conference on. (2005). IEEE, Volumn, (Year) III-457.

[37] Y. P. Kocak,S. Sevgen, Detecting and counting people using real-time directional algorithms implemented by compute unified device architecture. Neurocomputing, 248, (2017) 105-111.

CHAPTER 4. IN-SITU MONITORING OF ELECTROHYDRODYNAMIC INKJET PRINTING VIA SCALAR DIFFRACTION FOR PRINTED DROPLETS

Modified from a manuscript under review by Journal of Manufacturing Systems

Benjamin Lies[a], Xiao Zhang[a], Hao Lyu[b], Hantang Qin[a]

[a]Industrial and Manufacturing Systems Engineering Department, Iowa State University, Ames, Iowa, 50011, USA; [b]College of Mathematics and Physics, Qingdao University of Science & Technology, Qingdao, Shandong,266061, China

Abstract

Electrohydrodynamic inkjet (e-jet) printing is a technique which utilizes electrical forces to generate droplets in micro/nano scale using conductive inks. Currently, there is no procedure in place to measure the printed patterns without taking the sample away from the printer setup. Removal of the substrate from the printing stage during the e-jet printing process prevents any additional work from being performed on the sample. We investigated the application of scalar diffraction for the in-situ measurement and digital reconstruction of opaque material printed on transparent substrates. Measurement and characterization of the printed material can be achieved in-situ to alter printing condition in process for quality assurance. In order to accomplish the sample reconstruction, a digital recording of a scalar diffraction pattern in the image plane was employed in this paper with a magnification of 5x with the help of a combination of lenses. The reconstructed images were then compared to images captured by an offline high-resolution microscope. The results indicated a submicron accuracy of the feature radii. In addition to the quantitative measurements, this method also allows for the operator to view the overall form of the printed patterns. Our findings demonstrate an effective approach for in-situ monitoring of e-jet printing and printed

patterns, which could pave the way for the industrial application in printing testing field. This method may be used in conjunction with machine vision assisted filament detection to improve the process of the E-jet printing/Laser ablation hybrid system.

Introduction

As the need for flexible electronics grows rapidly, the fabrication of small electronic components in micro and nano scale has been significantly necessary [1]. Traditionally, etching and masks were used to fabricate these structures. These methods face drawbacks, however, namely poor customizability and high cost, which are difficult to overcome in order to achieve the high-resolution pattern [2]. Moreover, the requirement of a clean room environment further increases the difficulty of quick prototyping for electronic components and devices. Electrohydrodynamic jet (e-jet) printing is an emerging method for the fabrication of micro/nano structures in electronics and optical fields. This technique has the ability to print high-resolution patterns down to sub-micron with stable droplet generation in addition to fast fabrication for electronics (e.g., sensors) [3]. With further development of the e-jet printing technique, advanced fabrication of electronics became possible. Rogers [4] used e-jet printing to form patterns of quantum dots for light-emitting diodes. Our group [5] applied the e-jet printing technique to fabricate capacitive touch sensors and achieve sub-20 μm conductive pattern on a flexible insulating substrate. For better control of the e-jet printing process, many methods were proposed to improve the printing quality further. Dong [6-8] used modulated ac-pulse voltage to minimize the residual charge issue and overcame the long-predicted charge accumulation problem on highly insulating substrates. With better voltage control strategy, Mishara [9] demonstrated high-speed printing capability at 1 kHz with 3-5 μm droplet size for an aqueous ink and 1-2 μm for a photocurable polymer ink.

High-speed e-jet printing method had the additional advantage of reducing the line-pattern width. Phung [10] reported that the pattern width could be reduced from 20 μm to 4 μm by increasing the speed from 10 mm/s to 50mm/s.

In order to improve reliability and quality control of e-jet printing process, many approaches were explored to investigate the influence of printing and material parameters. Lee [11] investigated the effect of viscoelasticity of typical ink on Taylor cone formation using a two-model system. Han [12] applied the e-jet printing process for phase-change wax material; both experiment result and FEA models demonstrate agreement with each other. Ink characteristics played a large part in the final quality of printed patterns, and one such ink characteristic was the solvent used. Je [13] used silver nanoink for printing, which contained a low boiling point solvent, and the results were dots and lines with superior quality. However, it was difficult to monitor the results of these altered printing parameters. Many researchers focused on the image processing process to instruct the printing process such as Gardner [14] reported the operation of optical coherence tomography in a selective laser sintering system to monitor the surface feature of the printed part. Similar research has been done by Grasso [15], a method was proposed for detection and recognition of spatial defects during the selective laser melting process, but challenges remain under different frame rates at the same experimental setup. Imani [16] proposed image based method to collect nonlinearity, irregularity during the manufacturing process, which link the process parameters with in-process images. Wang et al. applied in-situ droplet inspection based on image analysis for liquid metal jet 3D printing, but not for printed parts [17]. In previous works, we [18] used machine vision to enable real-time monitoring of the e-jet printing process and the implementation of a feedback control system to achieve a higher quality

pattern. A similar machine vision system was used by Lee [19], who applied a vision algorithm to enable in-situ measurement of the e-jet printing process. Both of these vision processes monitored the Taylor cone formation, but they did not show the pattern printed on the substrate in real-time.

Currently, measurements of printed results are usually performed offline via an optical microscope or other similar metrology methods, which results in the removal of the substrate from the printing platform. Once the substrate has been removed, additional printing is impossible as realignment is difficult and most time is not feasible. An alternative new method for in-situ monitoring and characterization of such printed droplets is needed. Inkjet-based printing is a droplet driven process. The measurement of dot patterns (formed by droplets) is the key step before the realization of printing high quality patterns. Successful dot patterns could be used for micro/nano array patterning, and line patterns could contribute to the manufacture of devices such as wearable sensors. Laser diffraction system is flexible for measurement in various environments and robust for in-situ characterization. In this contribution, we demonstrated an approach using scalar diffraction for the in-situ measurement and digital reconstruction of e-jet printing. A digital recording of a scalar diffraction pattern in the image plane was employed to evaluate the printed results in process. This approach could open a new way for in-situ monitoring and characterization of e-jet printing.

Fabrication Setup: E-jet Printing Process

The experimental setup of e-jet printing was shown in

a. A commercial silver nanoink was used as the printing material for this experiment. A three-axis nano-positioning stage was used for the movement of the printer head and

substrate. During the printing, the movement in x and y direction was programmed in the horizontal plane for printing on the substrate. The z direction was programmed to obtain a desired standoff distance from the nozzle tip to the substrate. The positional resolution along the x and y direction was 50 nm, and the speed of lateral directional movement could vary from 0.001 mm/s to 20 mm/s. The substrate used as the printing platform was transparent (e.g., glass slides or PET films) and the standoff distance was set to 20 μm. A high electric potential was applied between the nozzle and substrate, with the voltage ranging between 500V to 1000V. The positive and negative electrodes of the voltage supplier were connected with the nozzle and the substrate, respectively. The diameter of the nozzle varied between 2 to 30 μm. With such small sizes, the surface tension of ink prevented droplet formation at the tip of the nozzle without a voltage supply. The electrical force drove the silver nanoink out of the nozzle onto the substrate and served as the primary force for stable jetting the material. A camera was used to monitor the region between the nozzle and the substrate. After the settlement of the nozzle on the system, the positive and negative electrodes of the voltage supply were connected with the nozzle and the substrate, respectively. Via control of process parameters (e.g., voltages, plotting speed, etc.), different sizes of silver droplets, dots, and lines were achieved, as shown in Fig. 1b.

In a traditional setup of e-jet printing, the camera shown in Fig. 1a was used to observe the region between the nozzle and the printing substrate, and to monitor the in-flight droplet behavior. The resolution of such optical zoom lens and camera could be as high as 2 μm with associated cost around $4000. However, this in-situ setup could not observe the pattern being printed. Aligning additional zoom lens system on the z stage increased extra load and reduced control resolution of the z-axis. This means that the operator could only

predict what the printed pattern would look like based on the printing parameters established beforehand using a traditional setup in Fig. 1a. These parameters included voltage, ink characteristics, standoff distance, translation speed, etc. Currently, the method to characterize the printed pattern was to remove the substrate from the printing stage and to conduct metrology offline using microscopy (SEM or optical). Removal from the stage eliminated the possibility for any additional future printing as there was no longer any point of reference and the small scale of the printing made realignment very difficult. Without an effective approach to recognize printed patterns in-situ or establish a point of reference for future alignment, quality control of e-jet printing would likely to remain difficult. In this paper, a scalar diffraction vision system was developed to resolve the challenge.

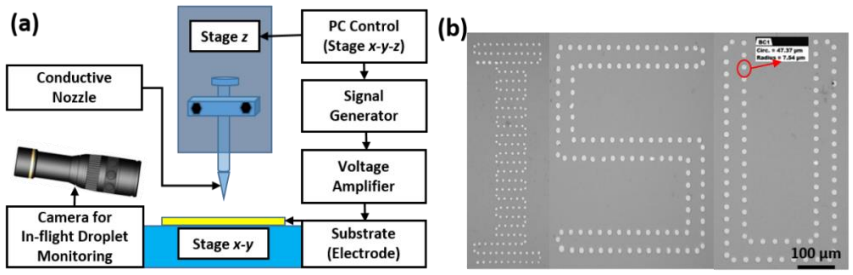

Fig. 1: (a) Schematic of e-jet printing, and (b) printed droplet patterns

Scalar Diffraction Vision System

The following scalar diffraction system was proposed to solve the challenges mentioned in previous sections regarding quality assurance and feature recognition for e-jet printing. Fig. 2a demonstrated the optical equipment location as it would relate to the e-jet printing setup and Fig. 2b showed the specifics of the components of the optical system setup.

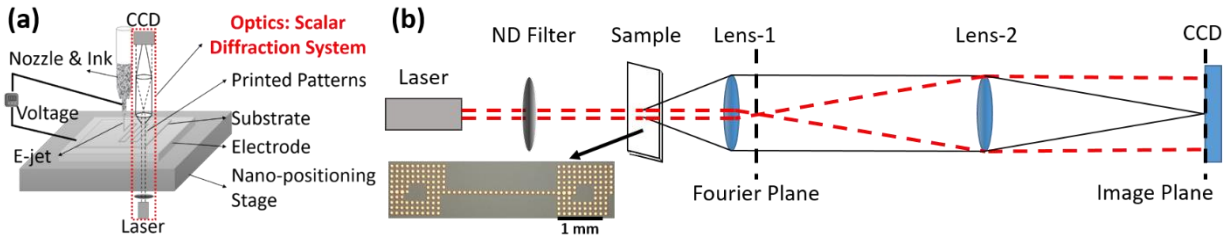

Fig. 2 : (a) Location of scalar diffraction system in e-jet printing setup, and (b) a schematic of the optical components for scalar diffraction

The laser as a light source used in this experiment was a 2 mW HeNe laser (wavelength 632 nm). The light then passed through a step neutral density (ND) filter. The magnitude of this filter was set such that the light incident on the CCD did not saturate the camera in order to preserve as much information as possible. The sample used in this experiment was silver nanoink printed on a transparent substrate via e-jet printing. The ink pattern was on the side opposite the incident light. Nemoto investigated the propagation of a Gaussian beam when passing through a dielectric material and determined that the waist size of the beam was unchanged when the light was normal to the surface of the substrate [20]. Some of the incident beam was then diffracted by the sample pattern, and the unscattered light passed through the transparent substrate (reference beam). The light diffracted due to the sample was then collimated by Lens-1 while also focusing the reference beam such that it could be represented by a single point in the Fourier plane. The Fourier plane was located behind Lens-1 at a distance equal to the focal length of Lens-1. The second lens, Lens-2, focused the collimated diffraction pattern resulting in the formation of the original image multiplied by the magnification that resulted from the objective lens system.

In this optical configuration, the digital sensor (e.g., charge coupled device CCD) could record an intensity pattern in either the Fourier plane or the image plane. Each of these planes had unique characteristics. The Fourier plane was observed after the incident light had

been diffracted by the sample and the resulting pattern was observed in the far field. In order to satisfy this far field condition, the diffraction pattern resulting from the light incident to the sample was collimated by a lens. This collimated pattern effectively described the pattern at infinity. This far-field pattern was typically referred to as the Fraunhofer regime, which was often described in terms of frequency. An example of a pattern recorded in the Fourier plane was shown in Fig. 3a. The image plane contained the reconstruction of the target sample in the spatial domain. An example of a pattern recorded in the image plane was shown in Fig. 3b.

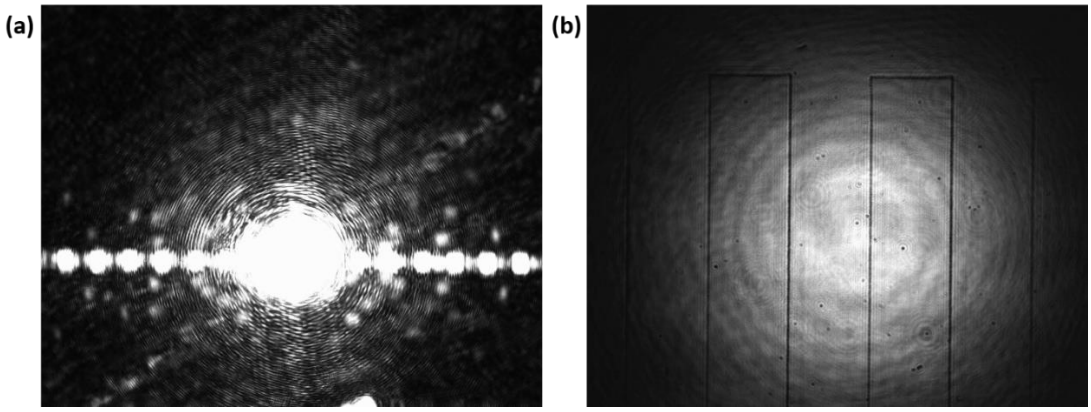

Fig. 3: Intensity distribution resulting from the printed pattern in the (a) Fourier plane and (b) image plane.

The Fraunhofer diffraction was described as the product of multiple approximations made in optics. Initially, the Huygens-Fresnel principle [21] was used to describe the diffraction of an object through the summation of small wavelets around the contour of an object or through an aperture. Later, the Fresnel-Kirchhoff integral theorem [22] expanded upon this theory through the implementation of Greens theorems [23]. The resulting equations were then approximated and categorized into two fields, Fresnel (near field) and Fraunhofer (far field) diffraction [24, 25]. The integrals associated with Fresnel diffraction were computationally challenging to solve outside of several known configurations. Thus,

the most straightforward approximation (computationally) was the Fraunhofer approximation, which utilized the Fourier transform to solve mostly due to the implementation of the Fast Fourier Transform (FFT) [26].

In the Fourier plane, the intensity distribution was a continuous function describing the frequency domain, but the device used for digital recording was discrete, which indicated that an insufficient sampling rate could result in aliasing of the data. In order to accurately recreate the continuous signal, the Nyquist-Shannon Sampling Theorem [27] should be implemented, which described the resolution restrictions due to predefined sensor parameters and the bandwidth limitations of the system. In addition to resolution limits imposed by discrete sampling, the intensity distribution in the Fourier plane had a couple of unwanted components. These components were the twin image and zero order image. There have been many methods proposed to isolate and differentiate the useful information from the twin and zero-order images. These methods required additional processing time however and should be avoided if possible.

The alternative to the Fourier plane was the image plane. The resolution of the image plane was not restricted by the Nyquist-Shannon Theorem as another lens was added which acted as a continuous inverse Fourier transform [28]. This resulted in an image of the sample plane multiplied by a magnification factor determined by the combination of lenses acting as the objective. As a result, recording in the image plane removed the need to experimentally or computationally remove the twin and zero-order image. The only calculations needed to interpret the image plane were the magnification due to the objective lens combination and the conversion from the image plane to the sample plane. ~~We derived the calculation equation based on the geometric optical theorem.~~

$$\frac{1}{f} = \frac{1}{d_o} + \frac{1}{d_i} \quad (1)$$

where f represented the focal length of the lens, d_o represented the distance from the object to the lens center, and d_i represented the distance from the lens to the resulting image.

The image resulting from the first lens was then used as the object for the second lens. The magnification of each lens depended on the distance at which the object was being observed, which was explained by Equation 2, where the negative sign represented the flipping or mirroring of the image with respect to the central axis joining the two lenses.

$$m_1 = -\frac{d_{i1}}{d_{o1}}, m_2 = -\frac{d_{i2}}{d_{o2}} \quad (2)$$

The effective magnification of the system would then be represented by M.

$$M = m_1 * m_2 \quad (3)$$

Equation 3 yielded the scale at which the image plane represented the sample plane. From this scale, tThe resolution in the image plane was determined as a function of effective magnification and the discrete sample sizing of the camera. The resolution of the camera and FOV regarding the sample plane could then be determined.

There were several factors which may limit resolution in the system. The diffraction of light as it passed through a lens was an unavoidable problem. This resolution limit was typically calculated and used as an ideal case. Equation 4 represented alternative theoretical resolution limit.

$$R = \frac{\lambda}{2NA} \quad (4)$$

where NA represented the numerical aperture of the objective lens, and λ was the wavelength of the laser. In our study, the objective lens had a numerical aperture of 1/9.8. This resulted in a resolution limit of 3.096 μm in the sample plane. The camera pixel

corresponded to an area of 0.92 μm in the sample plane. As a result, the resolution limitation was due to the diffraction. A resolution of 3 μm was small in comparison to the feature sizes of the sample. In this case, the limiting factor would be the camera itself.

Image Processing

E-jet printing could generate droplet and dot patterns on flexible and transparent substrates as shown in Fig. 1b. In this study, in order to utilize scalar diffraction system for quality assurance of e-jet printing, we fabricated the patterns with certain common defects (e.g., non-circularity, line coalescence, droplets connection, etc.). Imaging processing algorithms were developed to perform feature recognition and quality control.

Background Analysis

In the image plane, the unscattered light was magnified onto the camera in a Gaussian shaped intensity pattern. This Gaussian pattern was constant among all of the images, so it was essential to isolate and remove this pattern. Several images were taken when there was no printed silver dots on the substrate. The average between these images was used in order to reduce the noise caused by any dust that could be on the transparent substrate. The average was found using Equation 1,

$$\mathrm{B(x,y)} = \frac{\sum_{\mathrm{i=0}}^{\mathrm{n}} \mathrm{b_i(x,y)}}{\mathrm{n}} \tag{1}$$

where $B(x, y)$ represented the average pixel intensity for a given pixel. Each individual background image was represented by b_i where the number of images averaged was n. There were several perturbations which were consistent throughout all of the background images which did not require to be removed as they would remain in the sample image as well. In Fig. 4, a reducible disturbance has been circled in red for both images.

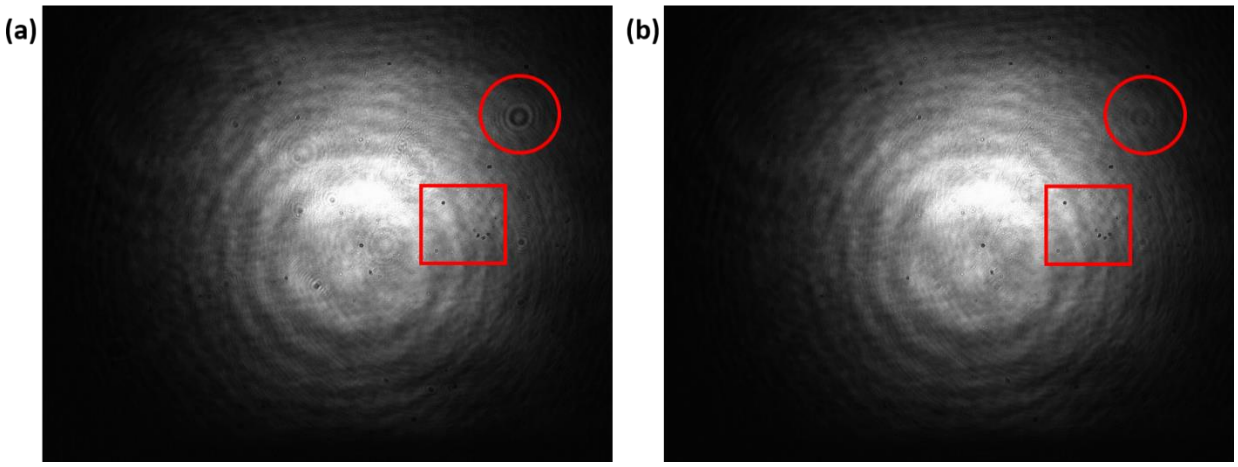

Fig. 4: (a) Singular background images with a unique disturbance (red circle) and several consistent disturbances (red square), and (b) average of several background images.

This was an example of how the intensity of the noise, which was inconsistent in the images (unique), was reduced. The square indicated several dots which were constant among all of the background images taken. This was dust on a lens or the camera itself which would be consistent in every image, thus remaining during the average procedure. The sample image was then subtracted from the average background image. The sample produced a darker pattern in the shape of the sample. Thus any negative values resulting from the subtraction could be set to '0'. This reduced noise as well as errors caused by an imperfect background image. The result was a sample pattern in greyscale without the reference beam. This was shown in Fig. 5a. The mathematical representation of this subtractive process was depicted in Equation 2.

$$D(x,y) = \max(B(x,y) - S(x,y), 0) \tag{2}$$

where $S(x,y)$ represented the individual pixels resulting from the light incident on the sample. This greyscale image contained sample information as well as some additional noise which resulted from the light passing through the finite lenses. The differentiation between these two categories was completed through binarization and filtering.

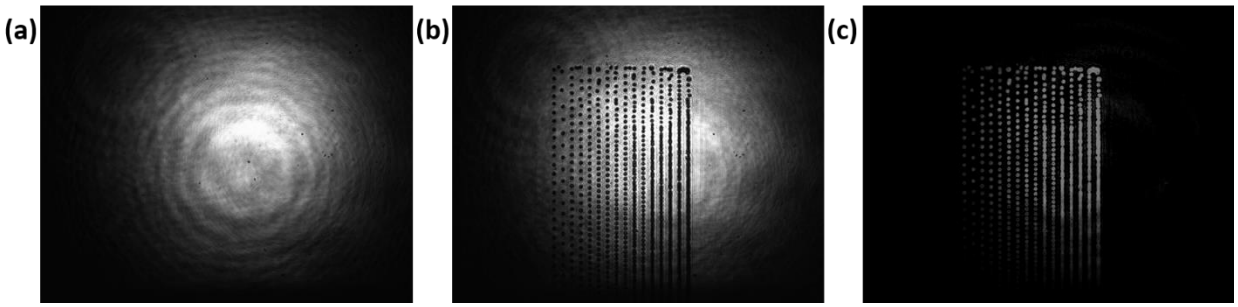

Fig. 5: (a) The average background image described by Equation 1, (b) the sample image, and (c) the result of the subtractive process described by Equation 2.

Binarization and Filtering

This magnified sample image contained locational and dimensional information for identification of reference point and evaluation of printing quality. In order to achieve real-time image processing, a binarization technique was used to convert the image from a greyscale into a black and white. The black represented the background while the white represented the pattern printed on the substrate. The binarization technique used in this experiment utilized local adaptive thresholding [29], which created several smaller windows inside the main image. Each neighborhood was approximately one eighth the size of the original image. In our algorithms, the mean of the neighborhood intensities was determined, and a sensitivity value was assigned by the user. The threshold for each neighborhood was a percentage of the mean value based on the sensitivity. The higher the sensitivity, the lower the threshold value resulting in more foreground pixels being identified. All of the intensity values of the pixels in the neighborhood were compared to this threshold. The greyscale image was then converted to black and white based on this threshold value. The value chosen for sensitivity was significant. For an image shown in Fig. 5c, a sensitivity that was too low could result in the loss of sample information (Fig. 5a), and a sensitivity that was too high could result in amplification of noise or saturation of the sample (Fig. 6b). It was also

observed that by increasing the number of pixels above the threshold, the size of a feature varied slightly.

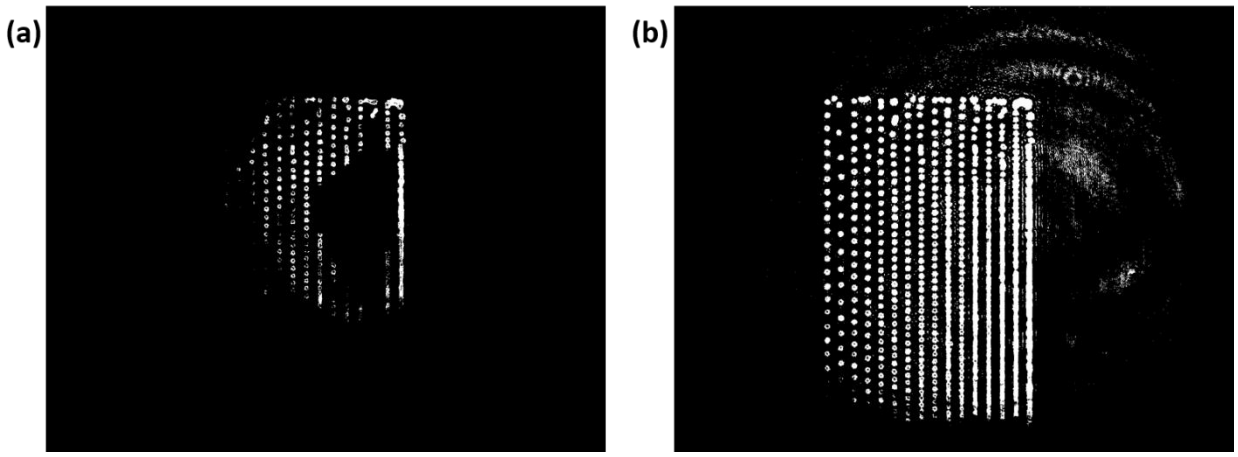

Fig. 6: (a) Image binarization using a low sensitivity (0.05, assigned by the user) resulting in information loss, and (b) a high sensitivity (0.55) resulting in the amplification of noise.

In order to maintain information without the inclusion of too much noise, a sensitivity somewhere in the middle must be chosen. Some noise could still be present, however, in order to remove the noise, a median filter was applied. This filter was able to remove speckle noise and to contract some features. The filtering approach in combination with the selection of the sensitivity could ensure that measured feature size was consistent. It was important to note that a median filter also had the capability to fill in holes and connect features that were one or two pixels away from each other. These influences were dependent on the filter size however and could be minimized by using a small filter size.

Cropping and Combining

The data from image plane could be binarized, but it has been observed that the areas with low contrast between the sample images and the background were not always reconstructed correctly, which limited the smart feature recognition of the system. In order to combat this, a region of interest (ROI) case study was established. The ROI was positioned over the area with the most significant contrast, the center of the Gaussian light. The ROI did

not move as the background light remains the same while the sample was moving during printing. In this work, the ROI has been established to be a 400 x 400 pixel region. The size was determined in order to maintain the high quality of information as well as a large physical area covered. The ROI of the sample that was used for further investigation was shown in Fig. 7. As mentioned in the previous section, the patterns were designed to reflect potential defects and to present different printing conditions.

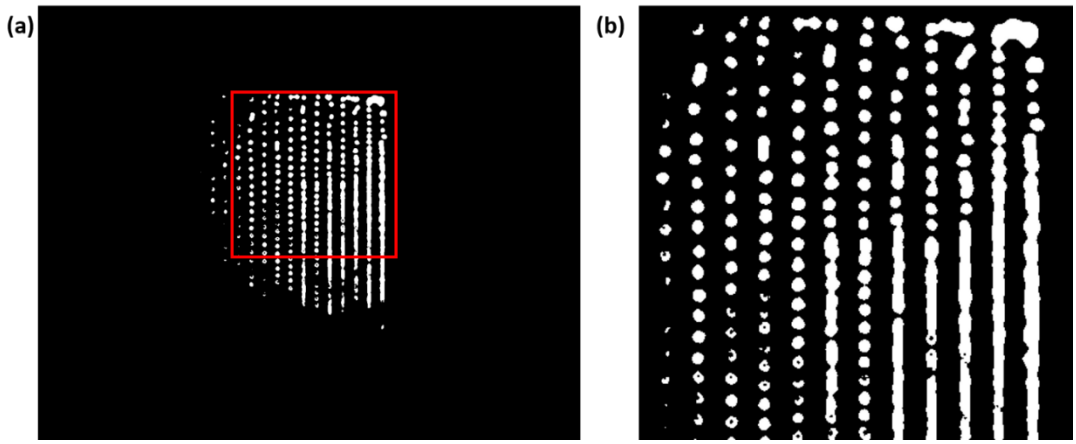

Fig. 7: (a) The full binarized image with the ROI identified, and (b) a full view of the ROI.

Once the region of interest has been established, several ROI could be combined in order to reconstruct the entire image. Currently, this was achieved through feature matching. An example of a combination of two ROI was shown in Fig. 8 in comparison to the same pattern under a digital microscope. As previously mentioned in the binarization and filter section, it could be seen that when the features were close to each other, some features were combined. This was caused by the selection of the binarization sensitivity or the work of the median filter.

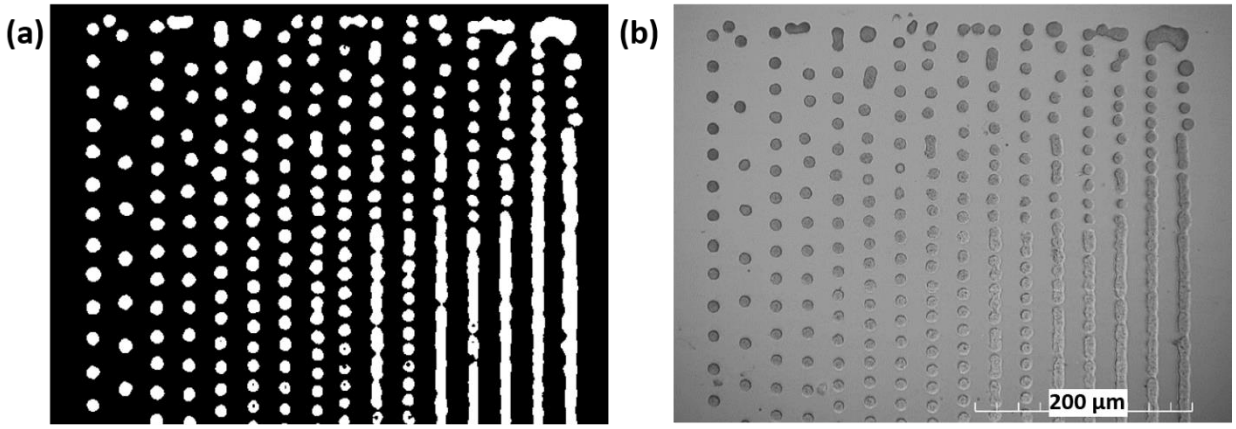

Fig. 8: (a) Combination of two ROI with its counterpart captured by (b) the microscope.

Circle Finding

After image reconstruction of the sample, the reconstructed images could then be analyzed to identify key features. The specific sample used in this study aimed to create a dot pattern so the feature identification approach will identify circles via circular "Hough" transform [30]. The method utilized the boundaries of each connected body. A circle was then applied to those candidates. These circles corresponded to a cone in the 3D Hough parameter space. The theory for the space could be represented by the following

$$(x-a)^2 + (y-b)^2 = r^2 \tag{3}$$

where (a, b) represented the circle center, and r represented the radius. The candidate pixels were represented by (x, y). The intersections of the resulting cones in the Hough space were collected in an accumulator matrix. The area was determined by the accumulator matrix which counted the intersections. From this matrix, the most suitable circle parameters were determined (a, b, r). This approach also required a sensitivity threshold that must be set by the user in addition to a radius range. With regards to the sensitivity, too low a sensitivity and the program would not be able to pick up a feature unless it was a near perfect circle, and too high a sensitivity and it would show false alarms (FA). An FA was determined to be anything

that was identified as a circle by the program which was not determined by the operator to be a circle, typically when multiple droplets were deposited too close resulting in one large figure. The limitation was due to the unique capability of a circular Hough transform which was the ability to find circles that were partially obscured by other objects or features. Examples of several sensitivity values were demonstrated in Fig. 9.

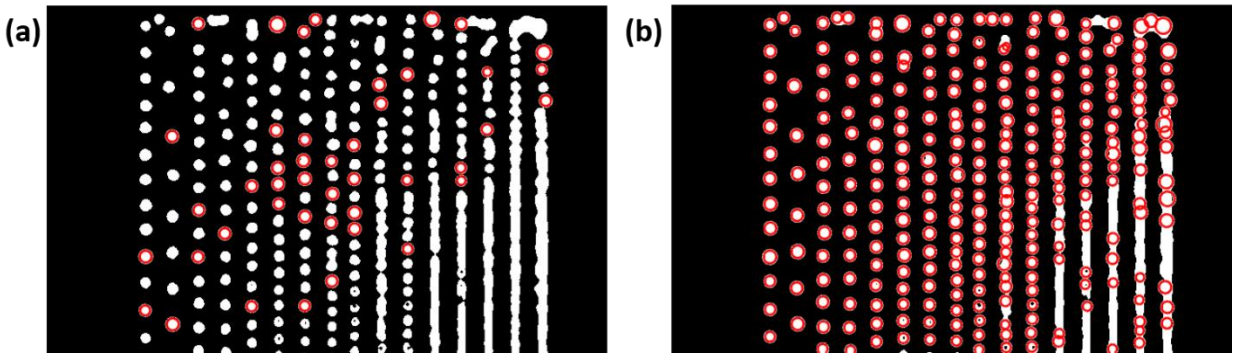

Fig. 9: The images with user defined circle sensitivity which was (a) too low, and (b) too high.

Once a circle has been identified, the radius and location of the circle were recorded. The accuracy, precision, and reliability of these location and size measurements would be compared with those measured by an optical microscope in the following section. In addition to the radius and location of the circle size, image processing could delete circles that overlapped. Overlapping circles can be seen in the top right corner of Fig. 9b. Depending on the preference of the operator, these could be removed in order to reduce the number of FA. Via the analysis of printed dots and image processing, the dot quality was easy to estimate, which could give direct guidance and feedback of printing parameter optimization.

Results and Discussions

In the previous section, the selection procedure for the binarization sensitivity, median filter size, and the circle finding sensitivity have been discussed. These constants

corresponded to the imbinarize(), medfilt2(), and imcirclefind() functions in Matlab. A range was set for each of these constants, and then each combination was processed and characterized. The binarization constant ranged from 0.15 to 0.25 in increments of 0.01. A smaller binarization constant resulted in the loss of dots and a larger constant resulted in additional noise and inflation of the dots (as shown in Fig. 6a-b). The median filter size ranged from 3 to 6 pixels in increments of 1. A smaller filter size resulted in poor noise reduction, and the larger filter size was more likely to combine dots and removed smaller dots entirely. The last constant, the circle finding sensitivity, ranged from 0.85 to 0.95 in increments of 0.01. Sensitivities smaller than 0.85 resulted in many "misses" and sensitivities higher than 0.95 resulted in a larger number of FA. In total, 484 combinations were tested. From these 484 variations, any combination which missed a dot was removed. In addition, the minimum circle sensitivity was used in order to reduce unnecessary false alarms. The result of these constraints were 18 different combinations as shown in **Error! Not a valid bookmark self-reference.**

Utilizing the combinations in Table 1, size distributions were created which represented the size distribution of the dots. These image processing size distributions (IPSD) were then compared with the microscope measured size distributions (MMSD).

Table 1. Different combinations of constants in imaging processing to test the scalar diffraction approach for identification of printed dot patterns.

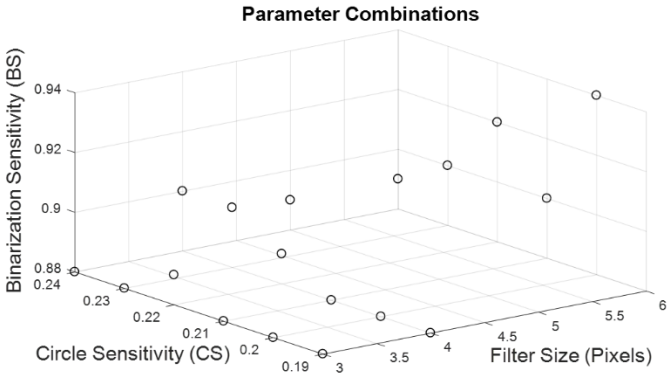

Filter Size	Binarization Constant	Circle Sensitivity	Filter Size	Binarization Constant	Circle Sensitivity
3	0.19	0.88	4	0.22	0.89
4	0.19	0.88	6	0.22	0.92
3	0.2	0.88	3	0.23	0.88
4	0.2	0.88	4	0.23	0.9
6	0.2	0.94	6	0.23	0.9
3	0.21	0.88	3	0.24	0.88
4	0.21	0.88	4	0.24	0.9
6	0.21	0.9	5	0.24	0.89
3	0.22	0.89	6	0.24	0.89

When comparing the IPSD and the MMSD, it was noted that the distributions appeared relatively normal, as shown in the probability density function in Fig. 10a. Thus, modeling them under the assumption that they were normally distributed that allowed for the computation of the mean and the standard deviation, both of which could be used to characterize the data as shown in Fig. 10b.

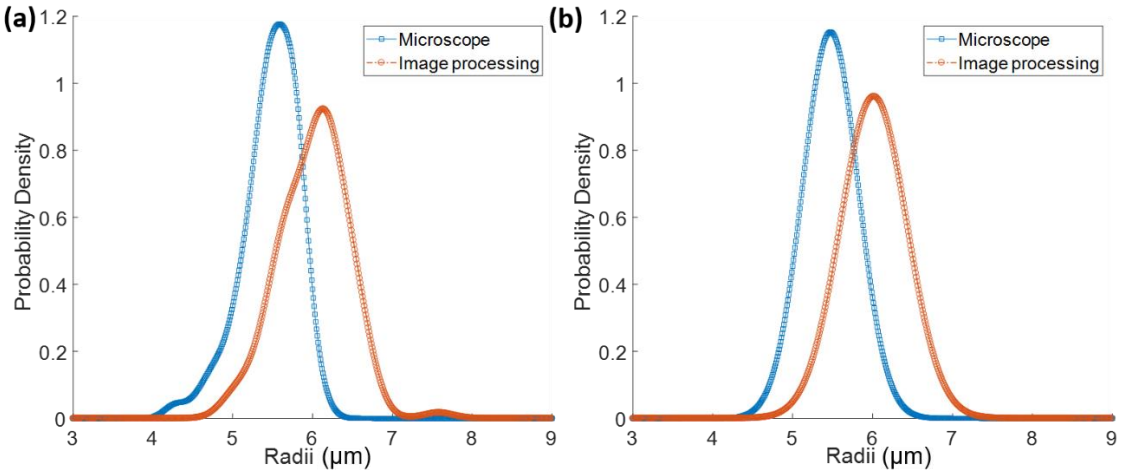

Fig. 10: (a) Radii comparison between the microscope and image processing algorithm, and (b) after normalization.

In addition, the number of false alarms could be easily determined as the remaining combinations have no “misses” and the number of “hits” was known. In the study, the

defining characteristics were the absolute difference between the IPSD μ1 and the MMSD μ2 (denoted Δμ), the absolute difference between the IPSD σ1 and the MMSD σ2 (denoted Δσ), and the number of false alarms. Each of these 18 combinations was then sorted 1-18 for each of these defining characteristics. The lower values being number 1, higher values being 18. Weight was given to each combination. The weight of each characteristic was subject to change depending on the needs of the operator and specific applications. As one example, **Error! Not a valid bookmark self-reference.** showed the results of an even weight applied to the Δσ, Δμ and the number of 'false alarms". The performance of each set of image processing parameters was then ranked for each sample group.

Table 2. Results of an even weight applied to the Δσ, Δμ and the number of "false alarms" for optimization of coefficients and constants.

Filter Size	Binarization Constant	Circle Sensitivity	Group 1	Group 2	Group 3	Group 4	Group 5	Group 6	**Total**
5	0.24	0.89	7	1	5	2	1	6	22
6	0.24	0.89	3	2	4	6	3	5	23
4	0.20	0.88	2	4	8	6	2	4	26
4	0.19	0.88	8	3	11	1	4	1	28
3	0.19	0.88	11	10	2	1	4	1	29
6	0.21	0.90	10	6	3	4	5	5	33
3	0.20	0.88	5	14	2	3	9	3	36
6	0.23	0.90	12	5	6	7	6	2	38
4	0.21	0.88	1	9	13	5	5	8	41
6	0.22	0.92	13	11	1	8	4	8	45
3	0.21	0.88	9	8	7	7	8	7	46
6	0.20	0.94	13	12	10	7	7	7	56
3	0.23	0.88	6	15	9	9	9	12	60
4	0.22	0.89	15	7	14	11	6	10	63
3	0.22	0.89	11	16	12	10	11	8	68
3	0.24	0.88	4	18	15	11	12	11	71
4	0.24	0.90	14	17	15	9	10	9	74
4	0.23	0.90	16	13	14	11	10	12	76

There were six different groupings of dots that were observed in this experiment. The first group was shown in the image processing section and can be entirely seen in Fig. 9. The remaining five groups utilized the same image processing routine using the 18 combinations of Filter Size, Binarization Constant, and Circle Sensitivity described in Table 1. Each combination of image processing parameters resulted in a Δμ and Δσ for each of the six dot groups. From these, the average absolute difference in the mean could be calculated and that the standard deviation of this average was computed as well. This average Δμ could then be plotted as a function of the binarization sensitivity as well as the filter size as shown in Fig. 11a and Fig. 11b respectively. The circle finding sensitivity was excluded as the lowest value resulting in no misses was chosen.

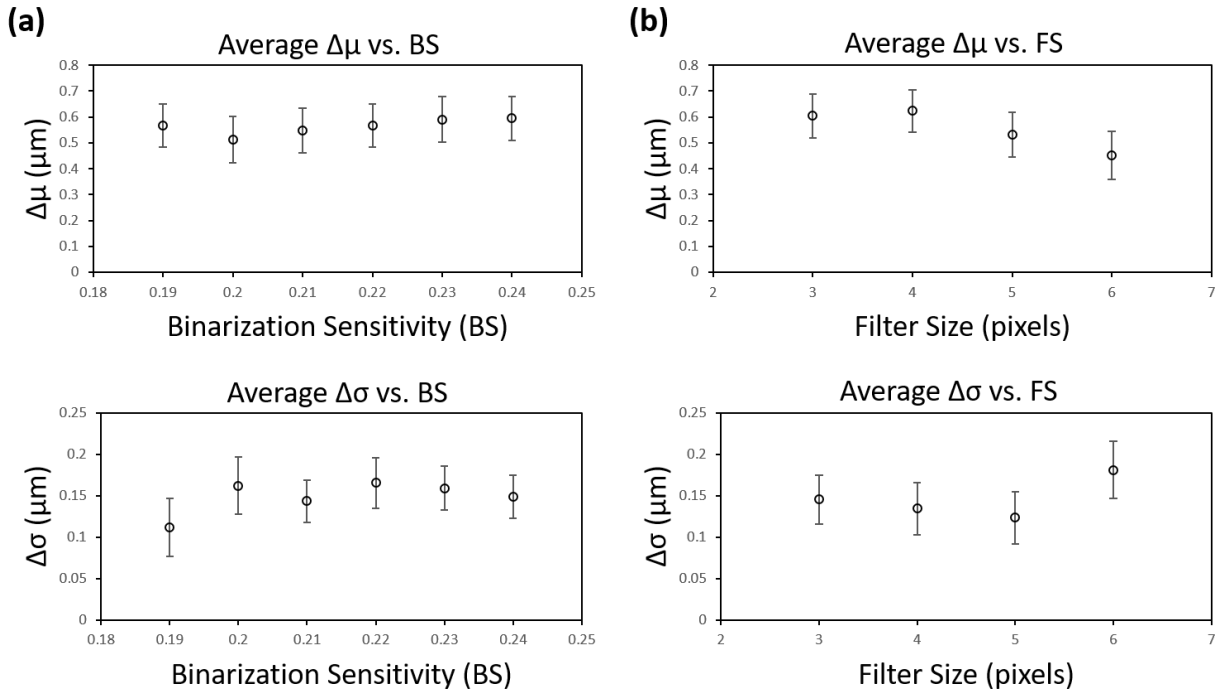

Fig. 11: Average value of (a) binarization sensitivity (BS), and (b) filter size (FS) comparison.

There were several trends in the values shown in Fig. 11. The accuracy and precision were a function of the binarization sensitivity and filter size. The size of these error bars was

representative of the standard deviation of the measured Δμ values, of the 18, with regards to binarization sensitivity and filter size respectively. The smaller the quantity, the more accurate the IPSD was to the MMSD. The smaller the error bars, the more consistent and therefore more precise the IPSD was. The results shown in Fig. 11 indicated that there was very little difference in the mean value of this distribution when selecting the binarization constant. When looking strictly at the binarization constant, it was only necessary that the operator chose a value that did not remove desired data points or generate too much noise when selecting the range. The constant should be large enough such that none of the dots were completely removed and small enough such that the noise was not an issue. In our study, a binarization constant of 0.19-0.24 were all sufficient with 0.2 being the most accurate. With regards to precision, 0.19 maintained the most similar standard deviation. When comparing the influence of the filter size, it should be noted that the smaller the filter size, the less accurate the resulting distribution was. When measuring the precision of the system, the largest filter size, 6, had the lowest precision. It was concluded that a filter size of 5 was best for the highest accuracy and precision combination. This filter size had the second highest accuracy and the best precision.

There were several ways that the data could be interpreted. First, the operator may be looking for settings which resulted in a particle size distribution most similar to the measurements given when measured via a microscope. It represented the most accurate settings or the settings which resulted in the smallest deviation (on average) from the actual distribution, which can be represented by the smallest Δμ values. Second, another measure of the quality of this methodology was the consistency of results between multiple sample areas. The consistency and the grouping of the differences was referred to as the precision of the

system, which was represented in this study, as the width of the curve, $\Delta\sigma$. This variability was not necessarily a negative factor as long as it was predictable and could be accounted for. Third, another measure was the number of false alarms present. In the case of feedback control for e-jet printing, false alarm measurement could be misleading and inconsistent systematically. Typically imperfections in this dot printing process were caused by the overlap of multiple dots. This circle detection method, by nature, found well-formed circles and those which were partially obscured, or in this study, overlapped. The operator could not tell if the dots were independent or connected as they were detected the same way in both cases. This made it difficult to draw a conclusion regarding the quality of the reproduction of the IPSD, with respect to the number of FA unless it was reviewed as it did not contain information regarding connectivity. The number of false alarms played a role in the mean and standard deviation of the size distribution; however, so it should not be ignored entirely. As a summary, it was ultimately up to the user and application to determine how each of these factors should be weighed when determining the "best" set of parameters to use for the image processing of scalar diffraction system.

The system has demonstrated good resolution. One of the advantages is the capability to measure sub-30 μm features to within several microns, but the overall performance is dependent on the parameters, not necessarily the system. The system is based on automated image processing with no differences among repeatable tests. We experimented with six different dot patterns and compared those to measurements collected via an optical microscope. The limitation of this system is the requirement of a transparent substrate which may restrict the application of this system in a wider area. Other than that, there are also many advantages. Due to the application of laser source, it has a strong capability to get rid

of environmental influences such as distance between object and laser source which enable the flexible setup of this system. The repeatability of this system could be ensured by the single wavelength of a stable laser source which supports the robustness of this laser diffraction system.

Conclusion

In this paper, a scalar diffraction system was developed for in-situ monitoring of printed patterns in e-jet printing. The approach had the capability to calculate the droplet size distribution of a sample without removal from the printing platform with magnification for micro/nano scale detection. The focus of this work is an in-process measurement technique, specifically for e-jet printing on transparent substrates. There are currently no such processes in use, which is an indication that this is the first application of such a system in this field. This work also has the capability to automate much/all of the inspection process. The measurements made during the image processing were consistent as long as the process parameters were chosen correctly. In addition to the measurements, the scalar diffraction system allowed an easy-setup and low-cost solution for the operator to monitor the quality of the printed sample, which was not currently feasible unless the sample was removed from the workspace and measured offline. The binarization constant should be chosen such that the noise was low while maintaining all of the feature data. The filter size should be chosen to remove the additional noise while maintaining the smaller features and avoiding the combination of dots. The circle finding sensitivity should be chosen such that the lowest number of false alarms were present. Several combinations of these parameters were demonstrated based on our printing setup, and the resulting difference in the size distributions was explained in details.

Our future work will be focusing on a digital twin system for e-jet printing based on metrology. Using the printing quality information as feedback control signals for e-jet printing, the approach could ensure dots were of the correct size for the correct feature and potentially spacing. Another significant contribution was that the approach enables the capability for easy system lineup with a reference dots on substrates when multiple layers of transparent substrates are required for higher dimensional fabrication.

References

[1] Galliker, P., Schneider, J., Eghlidi, H., Kress, S., Sandoghdar, V., and Poulikakos, D., 2012, "Direct printing of nanostructures by electrostatic autofocussing of ink nanodroplets," Nature communications, 3, pp. 890.

[2] Onses, M. S., Sutanto, E., Ferreira, P. M., Alleyne, A. G., and Rogers, J. A., 2015, "Mechanisms, capabilities, and applications of high-resolution electrohydrodynamic jet printing," Small, 11(34), pp. 4237-4266.

[3] Prasetyo, F. D., Yudistira, H. T., Nguyen, V. D., and Byun, D., 2013, "Ag dot morphologies printed using electrohydrodynamic (EHD) jet printing based on a drop-on-demand (DOD) operation," Journal of Micromechanics and Microengineering, 23(9), pp. 095028.

[4] Kim, B. H., Onses, M. S., Lim, J. B., Nam, S., Oh, N., Kim, H., Yu, K. J., Lee, J. W., Kim, J.H., and Kang, S.K., 2015, "High-resolution patterns of quantum dots formed by electrohydrodynamic jet printing for light-emitting diodes," Nano letters, 15(2), pp. 969-973.

[5] Qin, H., Cai, Y., Dong, J., and Lee, Y.S., 2017, "Direct printing of capacitive touch sensors on flexible substrates by additive e-jet printing with silver nanoinks," Journal of Manufacturing Science and Engineering, 139(3), pp. 031011.

[6] Qin, H., Dong, J., and Lee, Y.S., 2017, "AC-pulse modulated electrohydrodynamic jet printing and electroless copper deposition for conductive microscale patterning on flexible insulating substrates," Robotics and Computer-Integrated Manufacturing, 43, pp. 179-187.

[7] Wei, C., Qin, H., Ramirez-Iglesias, N. A., Chiu, C.P., Lee, Y.S., and Dong, J., 2014, "High-resolution ac-pulse modulated electrohydrodynamic jet printing on highly insulating substrates," Journal of Micromechanics and Microengineering, 24(4), pp. 045010.

[8] Wei, C., Qin, H., Chiu, C.P., Lee, Y.S., and Dong, J., 2015, "Drop-on-demand E-jet printing of continuous interconnects with AC-pulse modulation on highly insulating substrates," Journal of Manufacturing Systems, 37, pp. 505-510.

[9] Mishra, S., Barton, K. L., Alleyne, A. G., Ferreira, P. M., and Rogers, J. A., 2010, "High-speed and drop-on-demand printing with a pulsed electrohydrodynamic jet," Journal of Micromechanics and Microengineering, 20(9), pp. 095026.

[10] Phung, T. H., Kim, S., and Kwon, K.S., 2017, "A high speed electrohydrodynamic (EHD) jet printing method for line printing," Journal of Micromechanics and Microengineering, 27(9), pp. 095003.

[11] Yu, M., Ahn, K. H., and Lee, S. J., 2016, "Design optimization of ink in electrohydrodynamic jet printing: Effect of viscoelasticity on the formation of Taylor cone jet," Materials & Design, 89, pp. 109-115.

[12] Han, Y., Wei, C., and Dong, J., 2015, "Droplet formation and settlement of phase-change ink in high resolution electrohydrodynamic (EHD) 3D printing," Journal of Manufacturing Processes, 20, pp. 485-491.

[13] Shin, K.Y., Lee, S.H., and Oh, J. H., 2011, "Solvent and substrate effects on inkjet-printed dots and lines of silver nanoparticle colloids," Journal of Micromechanics and Microengineering, 21(4), pp. 045012.

[14] Singh, R., Zhang, X., Chen, Y., Zheng, J., and Qin, H., 2018, "In-situ real-time characterization of micro-filaments for electrohydrodynamic ink-jet printing using machine vision," Procedia Manufacturing, 17, pp. 45-52.

[15] Kwon, K.S., and Lee, D.Y., 2013, "Investigation of pulse voltage shape effects on electrohydrodynamic jets using a vision measurement technique," Journal of micromechanics and microengineering, 23(6), pp. 065018.

[16] Nemoto, S., 1989, "Waist shift of a Gaussian beam by a dielectric plate," Applied optics, 28(9), pp. 1643-1647.

[17] Miller, D. A., 1991, "Huygens's wave propagation principle corrected," Optics letters, 16(18), pp. 1370-1372.

[18] Kirchhoff, G., 1883, "Zur theorie der lichtstrahlen," Annalen der Physik, 254(4), pp. 663-695.

[19] Green, G., 1828, An essay on the application of mathematical analysis to the theories of electricity and magnetism, Wezäta-Melins Aktiebolag.

[20] Born, M., and Wolf, E., 2013, Principles of optics: electromagnetic theory of propagation, interference and diffraction of light, Elsevier: Chapter 8.

[21] Jenkins, F. A., and White, H. E., 1958, "Fundamentals of optics," American Journal of Physics, 26(4), pp. 272-272.

[22] Cooley, J. W., and Tukey, J. W., 1965, "An algorithm for the machine calculation of complex Fourier series," Mathematics of computation, 19(90), pp. 297-301.

[23] Shannon, C. E., 1998, "Communication in the presence of noise," Proceedings of the IEEE, 86(2), pp. 447-457.

[24] Coppola, G., Ferraro, P., Iodice, M., De Nicola, S., Finizio, A., and Grilli, S., 2004, "A digital holographic microscope for complete characterization of microelectromechanical systems," Measurement Science and Technology, 15(3), pp. 529.

[25] Bradley, D., and Roth, G., 2007, "Adaptive thresholding using the integral image," Journal of graphics tools, 12(2), pp. 13-21.

[26] Atherton, T. J., and Kerbyson, D. J., 1999, "Size invariant circle detection," Image and Vision computing, 17(11), pp. 795-803.

CHAPTER 5. LASER DIFFRACTION FOR IN-FLIGHT PARTICLE CHARACTERIZATION

Methodology

The objective of this work in this chapter is to investigate the feasibility of using laser diffraction for the assessment of particle size. The particles in this experiment range from 50-150 microns in size and remain stationary. From these stationary particles, a diffraction pattern will result from the interaction between the incident light and the sample. This diffraction pattern is characterized and the results are depicted bellow.

In order to investigate the sample characteristics, the diffraction pattern needs to be collected. This diffraction is a result of the light/matter interaction as the light passes around the sample. The system used to capture the diffraction pattern is shown in figure 1.

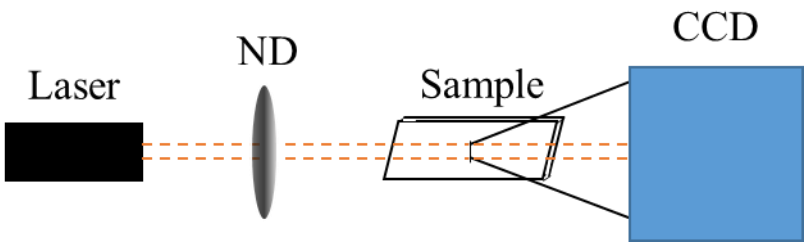

Figure 1: Laser diffraction setup for stationary particles.

The laser used in this experiment is a 2mW HeNe laser with a wavelength of 632.8 nm. A step ND filter is applied in the path of the laser in order to reduce the saturation of the incident beam on the CCD. The sample is the next component, containing a variety of patterns including a singular filament, dot and an array, all of which can be seen in figure 2. The last component is the CCD camera itself. The camera has a pixel size of 4.8x4.8 microns with a pixel count of 1280x1024.

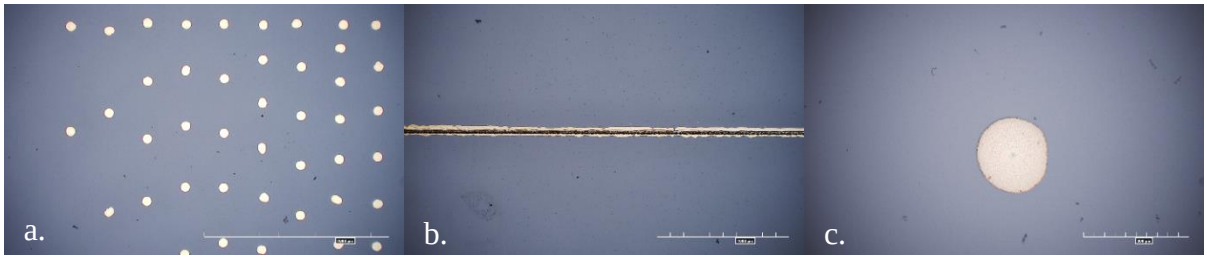

Figure 2: Optical microscope images of sample areas. a: An array of dots. b: A horizontal line. c: A singular large dot.

The average particle radius for the dots shown in figure 2a is 25.79 microns with a standard deviation of 0.67. The average line width as shown in figure 2b is 49.17 with a standard deviation of 5 microns. There are several inconsistencies throughout the line which lead to the larger deviation. The singular dot shown in figure 2c has an average radius of 69.81 microns. The next step is to decipher the information recorded by the CCD. This has been investigated in three ways.

The first investigation method is to compare the pattern which results from the diffraction to a pattern generated through code. The resulting diffraction pattern can be predicted when the sample space is known with regards to size and shape. In this work, the sample plane has been recreated and the predicted diffraction pattern has been generated for comparison. Depending on the distance between the sample and the CCD, the pattern can be represented by two distinct regions. The near field, also known as Fresnel diffraction [1], and far field, known as Fraunhofer diffraction [2]. Computationally, Fraunhofer diffraction is much easier and faster to solve. Thus, in this experiment, the CCD is placed in the far field. The equation used to determine the distance which constitutes the far field is shown by equation 1.

$$\frac{a^2}{\lambda D} \gg 1$$

Where a represents the aperture size, λ represents the wavelength of the light and D represents the distance between the sample and the CCD. In this case, “much greater than” will be represented by, one order of magnitude higher. Fraunhofer diffraction can be easily applied to the larger particles, therefore this experiment will focus on smaller particles.

The second way that the diffraction pattern can be interpreted is by taking the inverse Fourier transform of the resulting pattern. In the Fraunhofer regime, the diffraction pattern can be represented by the frequency space. This means that an inverse Fourier transform can be applied to the diffraction pattern and the result theoretically represents the sample plane. There are several known issues with this method however. One issue is the twin image problem, which means that the image resulting from the inverse Fourier transform is mirrored over the origin. This is difficult to remove, especially near the origin. The second issue is the DC component. There is typically a large DC component which occurs in the origin. The influence of both of these issues will be investigated.

The final method which can be used is exclusive to single aperture diffraction. The diffraction of a single circle or line can be represented through by equation 2.

$$\frac{I(\theta)}{I_0(\theta)} = \left(\frac{\sin\left(\frac{\pi b \sin(\theta)}{\lambda}\right)}{\frac{\pi b \sin(\theta)}{\lambda}} \right)^2$$

Where $\frac{I(\theta)}{I_0(\theta)}$ represents the relative intensity of the light, which is picked up by the CCD, θ is the angle of propagation, and b is the aperture size. This sinc squared function can be used in conjunction with a line of best fit program to estimate aperture size. It can observe a cross section of the diffraction pattern and from these intensity values, match the size that best fits the particle or line. The quality of the results for this single aperture measurement style is shown below.

Results and Discussion

The following images in figure 3 are the diffraction patterns resulting from the samples shown in figure 2. The patterns shown in column a were produced by the dot sample, column b patterns were produced by a line and column c patterns were produced by a singular dot. These patterns were collected with the camera 2 cm, 9.25 cm and 14.5 cm away from the sample. The diffraction patterns shown in the top row of figure 3 are a result of the 2 cm distance, these should not be compared during reconstruction as they are in the Fresnel region. This Fresnel region doesn't satisfy equation 1.

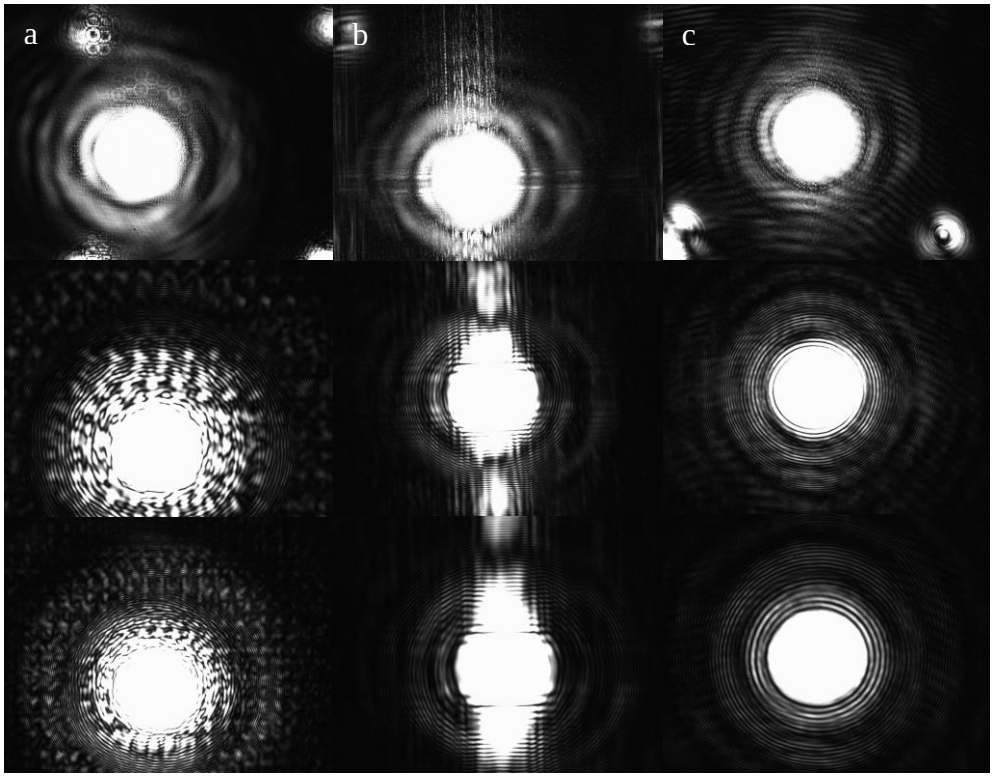

Figure 3: Diffraction patterns resulting from a dot array, single line, and single dot.

These Fraunhofer images will now be examined using method one. This method constitutes a recreation of the sample space and computing the diffraction pattern which results from it. This is done by using the fast Fourier transform of the sample space. The

recreation of samples 1, 2, and 3 are shown in figure 4a, the simulated diffraction patterns at a distance of 14.5 cm are shown in figure 4b.

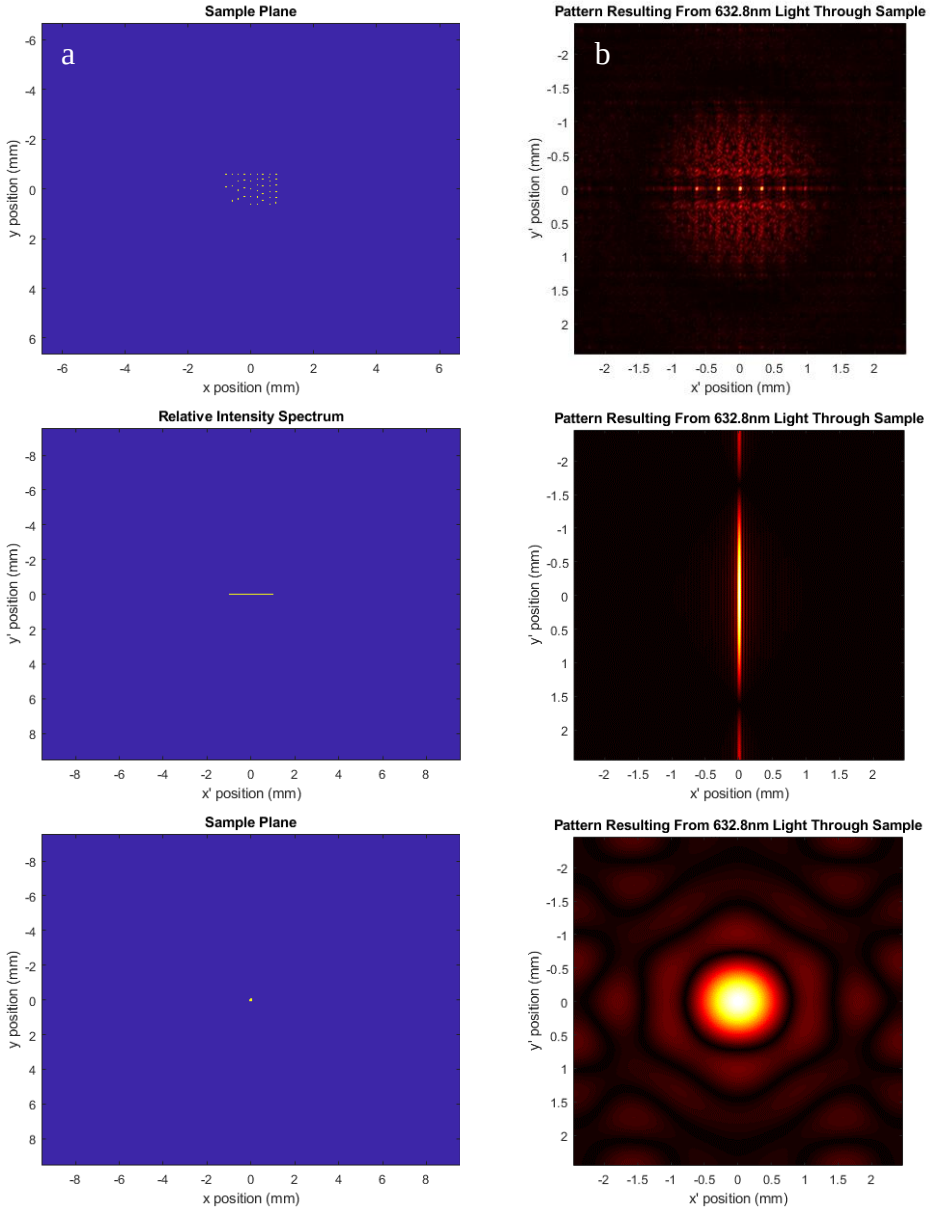

Figure 4: Column a represents a user created sample plane reconstruction of the dot array, single line, and single dot. Column b represent the resulting Fourier transforms.

The most notable difference, is the incident light that is present in the CCD images which are absent in the computed images. This extra light is due to the incident beam passing through the glass unobstructed by the sample. The opaque regions of the sample are small in

comparison to the transparent and thus most of the light passes through. This light saturates the camera which results in the loss of information. The next observation of note is resolution tradeoff between the sample space and the Fourier (CCD) space. The resolution of the CCD is predetermined which limits the resolution of the sample space. With an x and y resolution of 4.8 microns in the CCD plane, the resulting resolution in the sample plane is a function of the wavelength and distance of propagation. For example, the sample plane resolution for the dot array at 14.5 cm away is 18.6 microns and the resolution for the dot array at a distance of 9.25 cm is 11.9 microns. This makes it difficult or impossible to accurately represent the sample as there will be deviation from the real sample and the representation. This resolution limit causes the sample representation to be an incorrect size, integer multiples of the resolution, and incorrect shape, square pixels. This causes some deviation between the simulation and the experimental results.

The resulting patterns are similar, but due to the aforementioned issues, it is difficult to make a meaningful comparison between the recorded images and those produced through code. The incident light removes a lot of the necessary information in the center and due to the sample recreation limitations, the resulting pattern will never be “correct”. This does not mean that the results are worthless however. When comparing the results of the simulation with the collected diffraction patterns, they are quite similar. This is an indication that the diffraction pattern can indeed be represented by the Fourier transform, although it should not be used for measurement.

The second way to analyze the data is to convert the resulting CCD images into the sample space using an inverse Fourier transform, essentially the opposite of method 1. This analysis method also has the resolution conversion limitation in addition to twin image and

DC component issues mentioned in the method. The results of these inverse Fourier transformations are shown in figure 5.

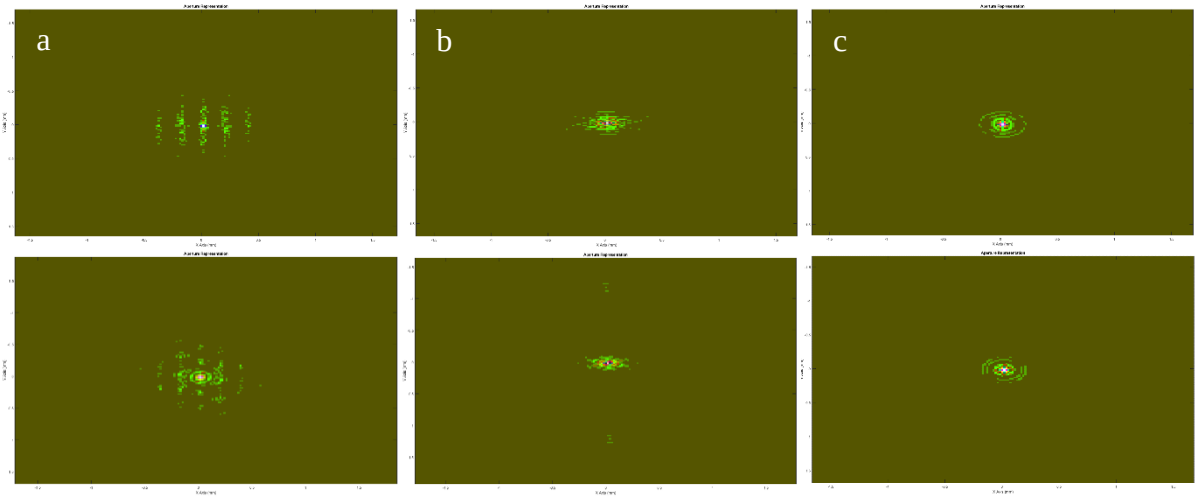

Figure 5: Column a shows the inverse Fourier transform of the diffraction pattern given by the dots at 9.25 (top) and 14.5 (bottom) cm respectively. Column b represents the line, and c represents the single dot.

The results show some form of the basic shape of the samples but the results are not nearly enough to constitute a measurement. The diffraction pattern resulting from the singular dot is the best quality but it also has several rings. These rings may be due to a number of sources. Perturbations in the pattern due to the transition from Fresnel to Fraunhofer can cause some high frequency noise which can be shown in the sample plane. In addition, the saturation due to the incident light must also be converted which can influence the magnitude of the resulting sample plane points. The sample reconstructions are positioned on the origin which contains the DC component. The reflection of the sample over the origin is also an issue as it is reflected on itself. This is primarily an issue for the dot pattern as the sample pattern is flipped on top of itself, resulting in a combination of the dots which further reduces the quality of the data. In this case, it is not possible to resolve the reflection caused by the twin image due to the proximity to the origin. None of the results

have a clear boundary and due to the issues above, as a result, this method is not advised for measurement or characterization purposes.

The final analysis method was then conducted which utilized the sinc2 function represented by equation 2. This can only be used for single particle/filament measuring. This program used a cross section of the intensity data. From this cross section, the saturated information was removed such that the fit would be less influenced by it. This influence cannot be completely removed however, in each of the intensity distributions shown in figure 6, there is a trend in the largest radian values, and this is the edge of the incident light saturation, which results in larger intensity values than the program predicts.

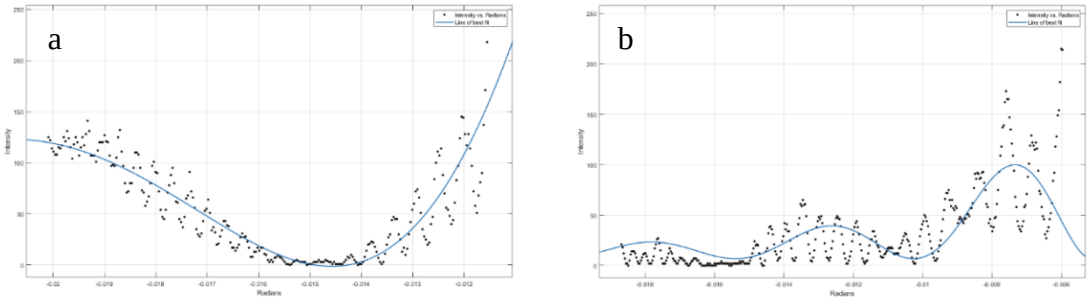

Figure 6: Cross sectional intensity data of a singular line (a) and dot (b).

From the diffraction pattern recorded for the line at 14.5 cm, the line diameter was determined to be 43.41 with an R^2 value of 0.83, in comparison to the optical microscope value of 49.17. The diffraction patterns resulting from the dot at a distance of 14.5 cm was determined to be 123.3 microns wide with an R^2 value of 0.47, in comparison to the optical microscope value of 139.62. The associated lines of best fit can be seen in figure 6. The fluctuations resulting from the transition from Fresnel diffraction to Fraunhofer diffraction can clearly be seen in figure 6. These fluctuations result in a large residual but the envelope of the intensity data aligns with the lines of best fit. This method makes a few assumptions, one of the assumptions is the center of the $sinc^2$ function. This cannot be known due to the

saturation of the system, and without it, the data may be skewed. This method also requires the operator to provide a guess as to what the size information is, without a reasonable guess, the size estimation will likely be poor. The last limitation of this method is the size and placement of the sensor in relation to the printed sample. As the particles get smaller, the angle of propagation increases, this can be seen using equation 2. This means that the camera needs to be relatively close to the sample to pick up the pattern, but it must not be too close otherwise it will be overcome by the Fresnel fluctuations. This coupled with the incident light saturation make it difficult to characterize small particles using this method, especially if the sample is unknown.

Conclusion

Although Fraunhofer diffraction can be used to model the diffraction pattern. The limitations of each of the three methods resulted in poor reconstructions. The resolution conversion, which resulted from the transition from the Fourier plane to the sample plane, limited the measurements in the sample plane. In addition, the unaltered incident light saturated a large section of the CCD, rendering a large portion of the sensor usable or misleading. This coupled with the fluctuations caused by the distance between the sensor and the sample, resulted in a poor sample characterization through all of the methods investigated.

These results lead the other to the follow recommendations. Beam shaping equipment should be used in order to reduce the incident light diameter. This would increase the amount of usable data recorded by the sensor. In addition to a smaller beam size, it is recommended that additional optical equipment be implemented such that the light diffracting from the sample and the unaltered incident light are offset by an angle or the unaltered incident light is

removed completely. This may be completed through the use of an interferometry or the addition of several lenses and an opaque stopper. The isolation of the sample diffraction light would result in more accurate data with regards to method one and two. The last recommendation is that the sensor used for this experiment is chosen based on the needs of the operator. The number of pixels and pixel size are constrains when converting from the Fourier plane to the sample plane which cannot be altered, thus the values are very important and should be chosen with care.

References

[1] Born, M., and Wolf, E., 2013, Principles of optics: electromagnetic theory of propagation, interference and diffraction of light, Elsevier: Chapter 8.

[2] Jenkins, F. A., and White, H. E., 1958, "Fundamentals of optics," American Journal of Physics, 26(4), pp. 272-272.

CHAPTER 6. GENERAL CONCLUSION

The aim of this work is to set-up the groundwork from which a hybrid manufacturing system may be implemented. The proposed hybrid system is comprised of laser ablation for material removal and Electrohydrodynamic inkjet printing for material addition. This system has potential to create flexible electronics at a very small scale. This work examines multiple methods for measurement of the E-jet printing process. This work also contains a literature review for the laser ablation of polymer films, the desired substrate for flexible circuits.

The literature review details the interaction between various laser types and common polymers. The most common materials are: Polytetrafluoroethylene (PTFE), Polyimide (PI), Polyethylene Terephthalate (PET), Polydimethylsiloxane (PDMS) and Poly Methyl Methacrylate (PMMA). The lasers included are: ArF laser, CO2 laser, Erbium laser, Iodine PALS doped fiber laser, KrCl laser, KrF laser, Nd: YAG, Nd: YVO4, Ti: sapphire laser, XeCl laser, and XeF laser. From this review, a basic understanding of laser ablation can be achieved, for a more detailed insight, one must read the associated references.

The high level trends observed are as follows. Melting can lead to a larger heat affected zone along with redeposition, cracks, and non-uniform material removal. Vaporization results in the formation of a plasma plume, which can interfere with the following pulse if the repetition rate is too high. Lower laser pulse duration reduces melting and increases vaporization. The longer the pulse, the more heat can propagate through the material. This propagation is also dependent on the thermal conductivity of the material. The ablation of the material is dependent on the wavelength of light used along with the absorption coefficient of the material. Typically polymers are more highly reactive to Ultraviolet wavelengths as this causes chemical breakdown as opposed to strictly thermal. In

addition to the absorption coefficient, molecular eight influences the rate of ablation. Typically, the higher the molecular weight, the lower the ablation rate.

As research continuous on laser ablation, quality, accuracy, and predictability of the technology will improve. With this, the optimal laser type and material can be selected to accommodate the needs of the user. In this case, this study can be used in combination with the necessity of the hybrid system in order to narrow down the laser type and material to be used for flexible electronics. After the selection has taken place, the E-jet printing system can be used for the rest of the process.

Currently, one of the biggest challenges to the E-jet printing process is the metrology and quality control. There are several different areas which can be observed and will ultimately reveal the information regarding the printing process and the resulting pattern. Starting in the Taylor cone, the jet emitted from the cone can be measured using a machine vision technology. This vision setup can be used in conjunction with image processing techniques in order to determine the filament diameter create a 3D representation of the jet. The diameter can be determined in real time while the 3D recreation must be done in post processing. The major constraint of this system is the camera /lens combination. These constraints limit this method to the micro scale.

The next observable feature is the plume formation which results when the jet breaks up resulting in particles smaller than the jet. The use of a simple scalar diffraction system was implemented to test the viability of detecting particles in an array or even singular particles. The particles in this experiment were stationary which is easier to measure than the plume particles. This technique faced major limitations however, namely: incident light saturation, resolution limitations, twin imaging issues, and the expansion of the diffracted

pattern by small particles. As a result, this simplistic measurement method should not be used for characterization of the plume.

Lastly, a process was proposed for the in-process measurement of the printed pattern. This process also uses scalar diffraction, but unlike the previous method, a lens is used to enact a continuous inverse Fourier transform on the diffraction pattern which eliminates the need to do it computationally. This work explains the image processing steps needed in order to recover the sample image and gives insight into the parameters associated with those processes. The results of this process is a digital recreation of the sample, particle size distribution, and location data for the printed particles. Depending on the parameters chosen, the accuracy and precision of the reconstruction and distribution size will vary. It is up to the user to determine what characteristics are most important and to choose the proper parameters for those needs.

In the future, the concurrent use of the machine vision system for filament size detection and the resulting pattern measurements can be achieved simultaneously in the E-jet printing process. By utilizing both of these methods, a better understanding of the process and parameter influence on the jetting and resulting pattern can be observed. In addition to the uses with regards to E-jet measurements. The system proposed in chapter 4 is one arm of an interferometric image plane digital holographic microscope. This digital holographic microscope has the capability to measure the thickness of semitransparent material. This system could then not only be used for the measurement of the inkjet printing system, but also the measurement of laser ablated polymers. The difference in optical path length of the light as it passes through the polymer can be characterized and the measurements of the ablated structures can be measured in process too. This would result in in-process

measurement capabilities for both the additive and subtractive processes of this hybrid manufacturing system with one measurement system.